TRACING THE IMPACTS OF MOUNT PINATUBO ERUPTION ON GLOBAL CLIMATE USING SPATIALLY-VARYING CHANGEPOINT DETECTION

Samantha Shi-Jun University of Illinois, Urbana-Champaign
Champaign, Illinois
Sandia National Laboratories
Albuquerque, NM

🔵 **Lyndsay Shand** *
Sandia National Laboratories
Albuquerque, NM

University of Illinois, Urbana-Champaign
Champaign, Illinois

Bo Li
University of Illinois, Urbana-Champaign
Champaign, Illinois
Sandia National Laboratories
Albuquerque, NM

August 13, 2025

ABSTRACT

Significant events such as volcanic eruptions can have global and long-lasting impacts on climate. These global impacts, however, are not uniform across space and time. Understanding how the Mt. Pinatubo eruption affects global and regional climate is of great interest for predicting the impact on climate due to similar events as well as understanding the possible effect of the Stratospheric Aerosol Injections proposed to combat climate change. While many studies illustrated the impact of the Pinatubo eruption on a global scale, studies at a fine regional scale are scarce. We propose a Bayesian spatially-varying changepoint detection and estimation method to trace the impact of Mt Pinatubo eruption on regional climate. Our approach takes into account the diffusing nature and spatial correlation of the climate changes attributed to the volcanic eruption. We illustrate our method and demonstrate its advantages over an existing changepoint detection method through simulations. Finally, we apply our method to monthly stratospheric aerosol optical depth and surface temperature data from 1985 to 1995 to detect and estimate changepoints following the 1991 Mt. Pinatubo eruption. Our results quantitatively characterize the spatial pattern of the eruption's impact on regional climate, complementing the previous studies on the global impact of the Pinatubo eruption.

1 Introduction

The Mount Pinatubo eruption in June 1991 is the largest volcanic eruption in recent history that injected nearly 20 megatons of sulfur dioxide into the atmosphere. The aerosol cloud resulting from the eruption encircled the globe for a few weeks, and global changes to the atmosphere, including a decrease in surface temperature in the northern hemisphere of about $0.5°$ C, were observed up to two years after the event [Self et al., 1996]. Studying the impact of volcanic eruptions is of high interest to the climate community for two main reasons. On the one hand, it helps improve

---

*corresponding author, lshand@sandia.gov

predictions of the anticipated impacts from new volcanic activities or other localized events such as wildfires. On the other hand, volcanic eruptions serve as natural examples of Stratospheric Aerosol Injection (SAI), a controversial proposed solar climate intervention to help cool the earth and reduce the impact of global warming through a global dimming effect [Robock, 2014]. Thus, a more comprehensive understanding of the impact of the Pinatubo eruption can shed new light on this radical technology against climate change.

Scientists have extensively studied how atmospheric properties were altered by the Mt. Pinatubo eruption. They found that the radiative forcing changes lasted for about three years [Stenchikov et al., 2009], leading to observed heating in the stratosphere of 2-3K [Labitzke and McCormick, 1992] and cooling of global surface temperatures of about 0.4 K [Dutton and Christy, 1992, Thompson et al., 2009]. Although there is a consensus that the eruption "caused" these global atmospheric changes, most published studies provided only qualitative evidence on a global scale. In this study, we attempt to quantitatively trace the impact of the Pinatubo eruption on aerosol optical depth and temperatures at a finer scale.

Since climate impacts from a volcanic eruption or a general SAI event are expected to cause sudden changes in regional climate, it is natural to use changepoints to trace the impact of an eruption at a regional scale. Changepoint detection methods aim to identify significant shifts in the underlying distribution of the data and have been employed to understand the impact of significant events on the environment. For instance, Hallema et al. [2017] used changepoint analysis to assess the impacts of wildland fires on watershed annual water yield, Robbins et al. [2011] developed a new changepoint detection method to identify changes in the tropical cyclone record in the North Atlantic Basin along with climate change over the period 1851–2008, and Tucker and Yarger [2023] found evidence of increased stratospheric temperature after the Mt. Pinatubo eruption using an epidemic changepoint model.

There have been many developments in changepoint detection in both univariate and multivariate settings, including two review articles [Reeves et al., 2007, Aminikhanghahi and Cook, 2017] and references therein. In particular, methods such as pruned exact linear time (PELT) algorithm [Killick et al., 2012] and product partition model (PPM) [Barry and Hartigan, 1992] have gained considerable popularity in the changepoint literature. In situations where time series are indexed by spatial locations, the change behavior of time series that are geographically nearby is likely to be similar due to spatial correlation. For such data, the direct application of traditional changepoint detection methods to each time series might overlook this spatial feature and is inadequate to exploit spatial correlation to improve changepoint detection and estimation.

To address this limitation, Majumdar et al. [2005] employed a Bayesian approach to detect various types of changepoints by incorporating spatial correlation. Additionally, Xuan and Murphy [2007] extended the PPM to account for the dependency structure in multivariate time series using sparse Gaussian graphical models. While these methods can handle spatial dependence among time series, they assume a common changepoint across all spatial locations, imposing a strong limitation on their application. Recently, a spatially-varying changepoint model was proposed by Berchuck et al. [2019] to monitor glaucoma progression in visual field data, where multivariate conditional autoregressive priors are used to model the spatial dependencies in the changepoints and the mean parameters. Their model assumed the data is temporally independent. Another related work is Wang et al. [2023], who developed a spatially-varying changepoint estimation method for functional time series observed over a spatial domain.

The changes in regional climate caused by the Pinatubo eruption or a general SAI event are expected to exhibit similarity at nearby locations due to spatial dependency. However, these changes are anticipated to occur at different times due to the diffusion of the injected aerosols across the globe and the atmospheric circulation. For particular variables such as the global aerosol optical depth (AOD) that measures the extinction of the solar beam by dust and haze, we expect that the time of the change will increase as the spatial distance from the event location increases, again due to the diffusion of aerosols. These unique characteristics of our problem render existing methods inadequate for our application. We, therefore, propose a novel space-time changepoint detection method that can identify when, where, and to what extent climate impacts have occurred following the 1991 eruption of Mt. Pinatubo while respecting the particular features of the SAI event.

Our approach departs from conventional methods by modeling changepoints as a spatial process and further allowing time-after-event of the changepoints to increase with the spatial distance from the event origin. By taking into account the spatial correlation of the data and the anticipated diffusion of the observed impact from the event location, our method is demonstrated to be more effective in capturing the spatial patterns of climate impacts associated with the SAI events. Since our focus is solely on tracing the impact of the Mt. Pinatubo eruption, we consider at most one change after the eruption. Compared to Majumdar et al. [2005], our method extends their model by allowing for spatially-varying changepoints. Furthermore, our approach performs both detection and estimation of changepoint at each location rather than only the estimation. Lastly, while most traditional methods focus on the mean shift, our method can detect changes in either the mean or variance, thus offering greater flexibility.

The rest of this paper is organized as follows. Section 2 describes the data and presents exploratory data analysis results. Section 3 introduces the model formulation and sampling procedure. In Section 4, we conduct extensive simulation studies to evaluate the performance of our proposed method. Section 5 demonstrates our methodology on AOD and surface temperature data observed around the time of the Mt. Pinatubo eruption. Finally, in Section 6 we provide a brief summary and discuss potential future work.

2 Data

As mentioned in Section 1, notable changes in aerosol optical depth (AOD) and surface temperatures caused by the Pinatubo eruption have been documented. While aerosols rapidly spread around the globe and experienced a near immediate and steep increase in magnitude following the eruption, changes in surface temperature were more subtle and took years to manifest. We consider the stratospheric AOD that measures the extinction optical thickness at 550nm[2], and the surface temperature[3], to evaluate the impact of the eruption. We obtained both data sets from the Modern-Era Retrospective analysis for Research and Applications, Version 2 (MERRA-2)[4].

The monthly AOD data ranges from January 1985 to December 1995, covering 132 time points in total. The data is over a 48×24 grid and covers the entire globe. Following Self et al. [1996], we exclude latitudes above 60°N and below 60°S in our analysis, resulting in $48 \times 16 = 768$ spatial locations. Figure 1(a) shows the AOD data on these 768 spatial grids. In general, the aerosol data exhibits a clear jump after the eruption, followed by an approximately linear decay in time toward its previous level. However, not all locations precisely agree on the jump time, likely due to the aerosol diffusion process. To enhance our analysis, we first remove the seasonality by applying Seasonal-Trend decomposition using LOESS (STL) [Cleveland, 1990] to AOD data at each location. Then, we estimate the temporal trend as a linear function of time using the historical data up to June 1991, the month of the eruption. If the estimated trend parameter is statistically significant at a 0.05 level, we remove the estimated trend for both pre- and post-eruption data. Assuming the trend between the month of eruption and the actual changepoint remains the same as in the pre-eruption period, this procedure roughly centers the time series before the changepoint so a constant mean can be assumed. Finally, we normalize the time series at each location by calculating the sample variance using data before June 1991 and use this number to achieve approximately constant variance across all locations.
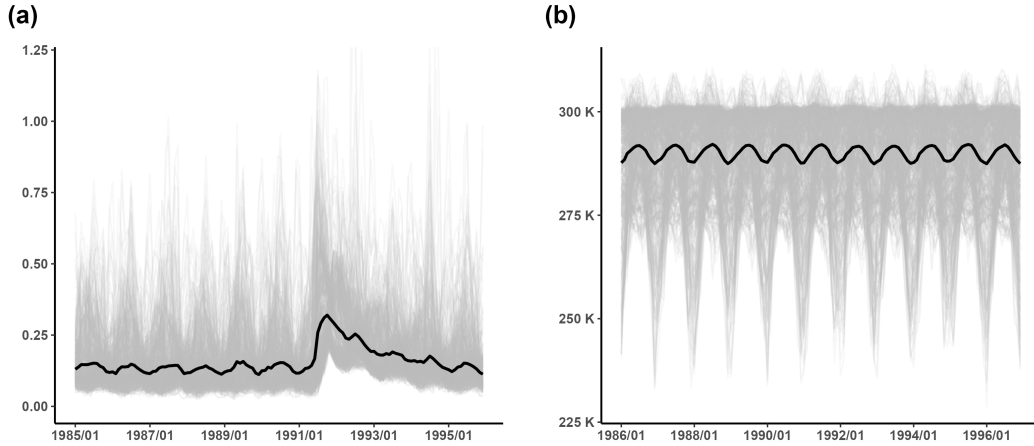

Fig. 1: Time Series of (a) stratospheric AOD data and (b) surface temperature data before preprocessing. Each grey curve represents a time series at a grid point. The black curve represents the global average.

The monthly surface temperature data, shown in Figure 1(b), also spans from January 1985 to December 1995 and is on the same 48×24 grid as the AOD data. In contrast to the AOD data, the impact of volcanic eruption on temperatures is indiscernible through simple visualization, suggesting a more subtle influence on temperatures, if any. When examining how temperature responds to a volcanic eruption, it is customary to study the temperature zonal mean indexed by latitude [Robock and Mao, 1995, Stenchikov et al., 2002, Gao et al., 2008]. Hence, we average temperatures over longitude for each of the 24 latitude bands given in the data and conduct the analysis on the latitudinal means. This reduces the

---

[2] referred to as "TOTEXTTAU" in Global Modeling and Assimilation Office (GMAO) [2015a]

[3] referred to as "tavg1_2d_slv_Nx" in Global Modeling and Assimilation Office (GMAO) [2015b]

[4] https://gmao.gsfc.nasa.gov/reanalysis/MERRA-2/

number of observations to 24, with each latitude representing a latitude band covering 7.5°. We employed the same procedure as for the AOD data to detrend and normalize temperature data. The processed zonal mean temperatures can be seen in Figure 8.

To evaluate our conjecture that changes in these climate variables vary spatially, we conducted exploratory data analysis on the global AOD data. At each grid location, we applied the Bayesian information criteria-based changepoint detection procedure, which is a well-established method for climate series [Reeves et al., 2007]. Figure 2 illustrates the heatmap of detected changepoints and estimated mean shifts at each grid location. Overall, the changepoints appear to be spatially-varying and clustered, as does the magnitude of change. Although a few locations show changepoints prior to 1991/06 that are apparently not due to the Mt. Pinatubo eruption, in general, the changepoints appear to spread latitudinally from the source of the eruption. This spatial pattern is consistent with what we expect from an eruption event, given the influence of strong zonal winds in the lower stratosphere that circulate the globe [Robock and Matson, 1983]. These results not only verify our conjecture but also provide guidance for the development of our methodology.
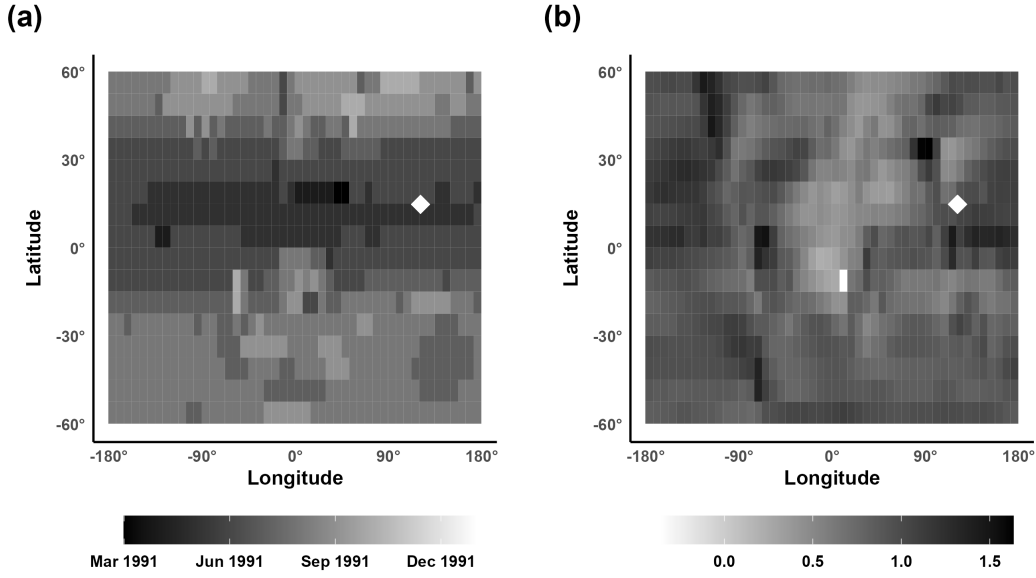

Fig. 2: (a) Heatmap of detected changepoints for AOD. Darker color indicates earlier change. (b) Heatmap of estimated change amount. Darker color indicates stronger magnitude of mean shift. The white diamond marks the location of Mt. Pinatubo.

3 Method

We propose a Bayesian hierarchical model to detect and estimate spatially-varying changepoints for spatiotemporal data. We model the likelihood of the data in the first level, provide the prior for the latent processes in the second level, and close the hierarchy by specifying priors and hyperpriors for all unknown parameters in the third level. We then discuss the challenges and the schemes of the Markov Chain Monte Carlo (MCMC) sampling algorithm used to estimate the proposed model.

3.1 Changepoint detection and estimation

Let $Y(\mathbf{s}, t)$ denote the observed climate variable at location $\mathbf{s} \in \mathbb{S}^2$ and time $t \in \mathbb{N}$, N be the total number of spatial locations, and M the total time points. We propose the following model for the spatiotemporal process $Y(\mathbf{s}, t)$ with possible mean and variance changes in time:

Level 1 The likelihood of the $Y(\mathbf{s}, t)$ process:

$$Y(\mathbf{s}, t) = \begin{cases} \mu_1(\mathbf{s}, t) + U(\mathbf{s}, t) + \epsilon_1(\mathbf{s}, t), & t \leq \tau(\mathbf{s}) \\ \mu_2(\mathbf{s}, t) + U(\mathbf{s}, t) + \epsilon_2(\mathbf{s}, t), & t > \tau(\mathbf{s}), \end{cases} \tag{1}$$

where $\tau(\mathbf{s})$ is the changepoint at location $\mathbf{s}$, $\mu_1(\mathbf{s}, t)$ and $\mu_2(\mathbf{s}, t)$ are the mean functions before and after changepoint, $U(\mathbf{s}, t)$ is a zero mean space-time correlated error process, and $\epsilon_1 \overset{iid}{\sim} N(0, \sigma_1^2)$ and $\epsilon_2 \overset{iid}{\sim} N(0, \sigma_2^2)$ are the before and after changepoint measurement errors. When $\tau(\mathbf{s}) = M$, it indicates the absence of changepoint at location $\mathbf{s}$ as the entire process is governed by a single model. To keep our model parsimonious and avoid potential identifiability issues, we assume a common spatiotemporal process $U(s, t)$ both before and after changepoint. This ensures that all changes will be attributed to mean and/or variance of measurement errors. This assumption also allows us to take advantage of the possible space-time separable covariance structure to facilitate the computation for spatiotemporal data. While Majumdar et al. [2005] allows for a change in the covariance structure by modeling the pre-changepoint error process as $U(\mathbf{s}, t) + V(\mathbf{s}, t)$ and the post-changepoint error process as $U(\mathbf{s}, t) + W(\mathbf{s}, t)$, their model assumes $\tau(\mathbf{s})$ as well as $\mu(\mathbf{s}, t)$ to be constant as a sacrifice to ensure identifiability. Since the primary interest for our data is to identify the spatially-varying changepoints while respecting the spatiotemporally-varying mean, we opt for a model that offers this flexibility.

As mentioned in Section 2, the data after preprocessing can be assumed to have a constant mean prior to the changepoint. Based on Figure 1(a), we assume a linear trend in time after changepoint. We also observe from Figure 2 that the change amount not only varies spatially but also tends to be clustered in space. To account for these features, we model the pre and post-changepoint mean processes, μ_1 and μ_2 respectively, as

$$\mu_1(\mathbf{s}, t) = \alpha_0 \tag{2}$$
$$\mu_2(\mathbf{s}, t) = \alpha_0 + \gamma_0(\mathbf{s}) + \gamma_1(\mathbf{s}) \cdot (t - \tau(\mathbf{s})) \tag{3}$$
$$= \alpha_0 + (\gamma_{0F} + \gamma_{0R}(\mathbf{s})) + (\gamma_{1F} + \gamma_{1R}(\mathbf{s})) \cdot (t - \tau(\mathbf{s})). \tag{4}$$

In (2) and (3), α_0 is the constant parameter representing the average global mean before the changepoint, $\gamma_0(\mathbf{s})$ is the mean shift at the time of the changepoint at location $\mathbf{s}$, and $\gamma_1(\mathbf{s})$ represents the slope after changepoint at locations $\mathbf{s}$. We further decompose $\gamma_0(\mathbf{s})$ and $\gamma_1(\mathbf{s})$ into a fixed and random components in (4). The fixed components γ_{0F} and γ_{1F} can be interpreted as the average mean shift and the average post-changepoint temporal trend across all locations that have a changepoint. The parameters $\gamma_{0R}(\mathbf{s})$ and $\gamma_{1R}(\mathbf{s})$ serve as spatial random effects to allow the mean shift and trend to vary spatially. To respect the spatial correlation of the magnitude of change and of the post-changepoint trend, we model $\gamma_{0R}(\mathbf{s})$ and $\gamma_{1R}(\mathbf{s})$ as a spatially correlated process.

Let $\mathbf{s}_0$ denote the location at which the change is first observed among all locations where we attempt to detect the changepoint, i.e., $\mathbf{s}_0 = \arg\min_\mathbf{s} \tau(\mathbf{s})$. If the influence of the volcanic eruption on the variable of interest diffuses from the event origin, $\mathbf{s}_0$ is usually either the event origin or some location nearby depending on what locations we consider for changepoint detection. We model $\tau(\mathbf{s})$ as the sum of two terms: the changepoint at the location $\mathbf{s}_0$, denoted by τ_0, and the temporal lag between changepoints at $\mathbf{s_0}$ and $\mathbf{s}$, denoted by $\Delta(\mathbf{s})$. Specifically, we have

$$\tau(\mathbf{s}) = \min\{M, \lfloor \tau_0 + \Delta(\mathbf{s}) \rfloor\}. \tag{5}$$

In theory, the "true" changepoint process can be defined as $\tau_0 + \Delta(\mathbf{s})$, where the temporal lags $\Delta(\mathbf{s})$ are continuous and take values in $(0, \infty)$. However, the observed changepoint is discrete and we are mainly interested in changepoints between 1 to M, so we take the floor sign and cap the value of changepoints at M. We require $\Delta(\mathbf{s}) \geq 0$ such that τ_0 is the earliest changepoint. This ensures that all other changepoints detected are either at or after τ_0 and thus not absolutely due to other unrelated events. We fix $\Delta(\mathbf{s}_0) = 0$ in our estimation because $\tau(\mathbf{s}_0) = \tau_0 = \min_\mathbf{s} \tau(\mathbf{s})$, as defined. Note that τ_0 takes discrete values in $\{1, \ldots, M\}$ and $\tau_0 = M$ implies that there is no changepoint at any of the locations. There are two main advantages of separating τ_0 from $\tau(\mathbf{s})$. First, it ensures that the changepoint at any location $\mathbf{s} \neq \mathbf{s}_0$ occurs strictly after the changepoint at $\mathbf{s}_0$, as any changepoint prior to τ_0 would be due to another event that is not of our interest. Second, we can model $\Delta(\mathbf{s})$ as a continuous process with a spatial correlation structure to reflect the spatial pattern observed in Figure 2(a) while keeping τ_0 as a discrete variable. The discrete parameter τ_0 can help us easily test if it is the case that no changepoint ever occurs at any of the locations and incorporate prior knowledge about the possible range of date at which the change caused by the eruption was first observed.

We further assume $\boldsymbol{\Delta} = (\Delta(\mathbf{s}_1), \ldots, \Delta(\mathbf{s}_N))^T$ follow a log normal process with mean $\mathbf{X}\boldsymbol{\beta}$ and covariance matrix $\boldsymbol{\Sigma}_\Delta$, where $\mathbf{X}$ is the $N \times 2$ matrix of spatial lags from each location $\mathbf{s}$ to the location $\mathbf{s}_0$, with the ith row of X given by $(\text{lon}(\mathbf{s}_i) - \text{lon}(\mathbf{s}_0), \text{lat}(\mathbf{s}_i) - \text{lat}(\mathbf{s}_0))$, and $\boldsymbol{\beta}$ is the 2-dimensional vector with each component representing the rate of diffusion in longitude and latitude, respectively. Allowing $\Delta(\mathbf{s})$ to increase with the distance from $\mathbf{s}_0$ in an anisotropic manner reflects the nature of the physical process shown in Figure 2 that the eruption diffuses at a different rate along the longitude and latitude, but in any direction, it takes a longer time for the eruption impact to reach a specific location that is further away from the event origin.

Let $\boldsymbol{\gamma}_{0R}$ and $\boldsymbol{\gamma}_{1R}$ be the vector of $\gamma_{0R}(\mathbf{s}_i)$ and $\gamma_{1R}(\mathbf{s}_i)$ for $i = 1, \ldots, N$, respectively. Let $\mathbf{U}$ be the vector stacking up all $U(\mathbf{s}_i, t_j)$ for $i = 1, \ldots, N$ and $j = 1, \ldots, M$, and let $\log(\boldsymbol{\Delta})$ be the vector of element-wise logarithms of $\boldsymbol{\Delta}$. In our next level of the hierarchical model, we provide priors for the latent processes in model (1).

Level 2 Latent processes:

$$\boldsymbol{\gamma}_{0R} \sim N(\mathbf{0}, \boldsymbol{\Sigma}_{\gamma_0}),$$
$$\boldsymbol{\gamma}_{1R} \sim N(\mathbf{0}, \boldsymbol{\Sigma}_{\gamma_1})$$
$$\mathbf{U} \sim N(\mathbf{0}, \boldsymbol{\Sigma}_{\mathbf{U}}),$$
$$\log(\boldsymbol{\Delta}) \sim N(\mathbf{X}\boldsymbol{\beta}, \boldsymbol{\Sigma}_{\Delta}).$$

For computational simplicity, we assume that $\boldsymbol{\Sigma}_U$ has a separable space-time covariance structure with an exponential covariance function in both space and time, i.e. $\boldsymbol{\Sigma}_{\mathbf{U}} = \sigma_U^2 \mathbf{R}(\phi_U) \otimes \mathbf{R}(\psi_U)$, where the (i, j)th element of $\mathbf{R}(\theta)$ is $R(\theta)_{ij} = \exp(-\theta h)$ for a distance h either in space or time, and $\otimes$ is the Kronecker product. Since our data spans the entire globe, we employed the great circle distance as the distance metric for the spatial correlation matrix. While a positive definite covariance function defined on Euclidean space may not necessarily be valid on spheres, the exponential covariance function has been shown to be valid on spheres when the Euclidean distance is replaced with the great circle distance. [Gneiting, 2013, Huang et al., 2011]. We assume $\boldsymbol{\Sigma}_{\gamma_0} = \sigma_{\gamma_0}^2 \mathbf{R}(\psi_{\gamma_0})$, $\boldsymbol{\Sigma}_{\gamma_1} = \sigma_{\gamma_1}^2 \mathbf{R}(\psi_{\gamma_1})$ and $\boldsymbol{\Sigma}_{\Delta} = \sigma_{\Delta}^2 \mathbf{R}(\psi_{\Delta})$, where $\mathbf{R}(\psi_{\gamma_0})$, $\mathbf{R}(\psi_{\gamma_1})$ and $\mathbf{R}(\psi_{\Delta})$ are also governed by an exponential covariance function with great circle distance.

3.2 MCMC Sampling

To describe the details of our sampling, we first write Model (1) in a matrix form. Let $\mathbf{1}_{\tau}^{+}$ be a MN-length vector of 0's and 1's, where 1 indicates that the corresponding time index in $Y(\mathbf{s}_i, t_j)$ is greater than $\tau(\mathbf{s}_i)$. Let $\mathbf{1}_{\tau}^{-} = \mathbf{1}_{MN} - \mathbf{1}_{\tau}^{+}$ be the vector of pre-changepoint indices. Then, Model (1) can be written as

$$\mathbf{Y} = \boldsymbol{\mu}_{\tau} + \mathbf{U} + \boldsymbol{\epsilon}_1 \circ \mathbf{1}_{\tau}^{-} + \boldsymbol{\epsilon}_2 \circ \mathbf{1}_{\tau}^{+}, \tag{6}$$

where

$$\boldsymbol{\mu}_{\tau} = \boldsymbol{\mu}_1 \circ \mathbf{1}_{\tau}^{-} + \boldsymbol{\mu}_2 \circ \mathbf{1}_{\tau}^{+}, \tag{7}$$

where $\circ$ denotes the Schur product operator, and $\boldsymbol{\mu}_1, \boldsymbol{\mu}_2, \boldsymbol{\epsilon}_1, \boldsymbol{\epsilon}_2$ denote the MN-length vector of $\mu_1(\mathbf{s}_i, t_j)$, $\mu_2(\mathbf{s}_i, t_j)$, $\epsilon_1(\mathbf{s}_i, t_j)$ and $\epsilon_2(\mathbf{s}_i, t_j)$ for $i = 1, \ldots, N$ and $j = 1, \ldots, M$. Let $\boldsymbol{\tau}$ be the vector of $(\tau(\mathbf{s}_1), \ldots, \tau(\mathbf{s}_N)^T)$. The full conditional likelihood of $\mathbf{Y}$ given $\mathbf{U}, \boldsymbol{\tau}, \boldsymbol{\mu}_1, \boldsymbol{\mu}_2, \sigma_1^2, \sigma_2^2$ is

$$f(\mathbf{Y}|\cdot) \propto |\boldsymbol{\Sigma}_Y|^{-1/2} \exp\left(-\frac{1}{2\sigma_1^2 \sigma_2^2}(\mathbf{Y} - \boldsymbol{\mu}_{\tau} - \mathbf{U})^T \boldsymbol{\Sigma}_Y^{-1}(\mathbf{Y} - \boldsymbol{\mu}_{\tau} - \mathbf{U})\right), \tag{8}$$

where $\boldsymbol{\Sigma}_Y = \sigma_2^2 \text{diag}(\mathbf{1}_{\tau}^{-}) + \sigma_1^2 \text{diag}(\mathbf{1}_{\tau}^{+})$ is a diagonal matrix of pre and post-changepoint measurement variances. Alternatively, integrating out $\mathbf{U}$ gives us

$$f(\mathbf{Y}|\cdot) \propto |\boldsymbol{\Sigma}_Y|^{-1/2} \exp\left(-\frac{1}{2\sigma_1^2 \sigma_2^2}(\mathbf{Y} - \boldsymbol{\mu}_{\tau})^T (\boldsymbol{\Sigma}_Y + \boldsymbol{\Sigma}_U)^{-1}(\mathbf{Y} - \boldsymbol{\mu}_{\tau})\right). \tag{9}$$

There are two main challenges in MCMC sampling for our model. First, Section 1 of the Supplement [Shi-Jun et al., 2023] shows that obtaining the posterior for $\mathbf{U}$ involves inverting the covariance matrix $\boldsymbol{\Sigma}_Y^{-1} + \boldsymbol{\Sigma}_U^{-1}$. If $\boldsymbol{\Sigma}_Y$ is a constant diagonal matrix, then because $\boldsymbol{\Sigma}_{\mathbf{U}}$ is separable we can sample $\mathbf{U}$ using eigendecompositions of $M \times M$ and $N \times N$ matrices instead of having to factorize a $MN \times MN$ covariance matrix [Stegle et al., 2011]. However, (8) shows that the matrix $\boldsymbol{\Sigma}_Y$ involves vectors $\mathbf{1}_{\tau}^{-}$ and $\mathbf{1}_{\tau}^{+}$ which depends on $\tau(\mathbf{s})$, and thus is not a constant diagonal matrix. As a consequence, we have to invert a $MN \times MN$ covariance matrix. This significantly amplifies the computational cost associated with sampling $\mathbf{U}$. Secondly, sampling both $\mathbf{U}$ and $\boldsymbol{\mu}_{\tau}$ can in practice lead to an identifiability issue, since both $\mathbf{U}$ and $\boldsymbol{\mu}_{\tau}$ have the potential to capture the trend in the data. While integrating out $\mathbf{U}$ from the model could solve these problems, retaining $\mathbf{U}$ is more desirable from a computational perspective. This stems from the fact that $\mathbf{Y}$ is no longer conditionally independent when the conditioning on $\mathbf{U}$ is removed, as indicated by the non-diagonal covariance matrix $\boldsymbol{\Sigma}_Y + \boldsymbol{\Sigma}_U$ in (9). Consequently, sampling other parameters whose full conditionals involve the likelihood of $\mathbf{Y}$ becomes significantly more intricate.

To address the first issue, we propose a simple but effective approach. We assume, without the loss of generality, that the variance increases after the changepoint and write the post-changepoint measurement error as $\boldsymbol{\epsilon}_2 = \boldsymbol{\epsilon}_1 + \boldsymbol{\epsilon}_{\gamma}$, where $\boldsymbol{\epsilon}_{\gamma} \overset{iid}{\sim} N(0, \sigma_{\gamma}^2)$ is a vector of white noise independent of $\boldsymbol{\epsilon}_1$. Then, we can rewrite $f(\mathbf{Y}|\cdot)$ in (8) as

$$f(\mathbf{Y}|\cdot) \propto \sigma_1^{MN} \exp\left(-\frac{1}{2\sigma_1^2}(\mathbf{Y} - \boldsymbol{\mu}_{\tau} - \mathbf{U} - \boldsymbol{\epsilon}_{\gamma} \circ \mathbf{1}_{\tau}^{+})^T (\mathbf{Y} - \boldsymbol{\mu}_{\tau} - \mathbf{U} - \boldsymbol{\epsilon}_{\gamma} \circ \mathbf{1}_{\tau}^{+})\right) \tag{10}$$

Ordinary Gibbs Sampler   **Partially Collapsed Gibbs Sampler**

Ordinary Gibbs Sampler
Step 1: $\tau \sim p(\tau\|Y, U', \theta', \alpha')$
Step 2: $\theta \sim p(\theta\|Y, U', \alpha', \tau)$
Step 3: $\alpha \sim p(\alpha\|Y, U', \theta, \tau)$
Step 4: $U \sim p(U\|Y, \alpha, \tau, \theta)$

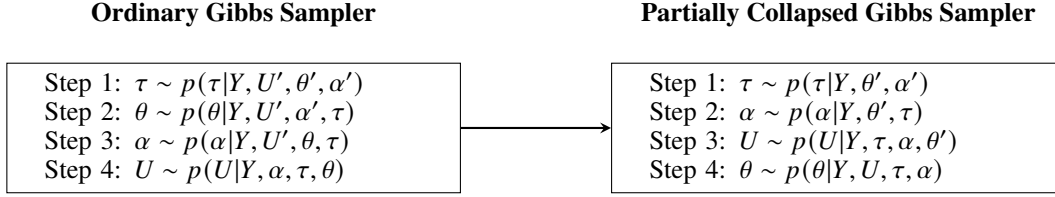| Partially Collapsed Gibbs Sampler |
| --- |
| Step 1: $\tau \sim p(\tau\|Y, \theta', \alpha')$ |
| Step 2: $\alpha \sim p(\alpha\|Y, \theta', \tau)$ |
| Step 3: $U \sim p(U\|Y, \tau, \alpha, \theta')$ |
| Step 4: $\theta \sim p(\theta\|Y, U, \tau, \alpha)$ |

Fig. 3: Sampling procedure for Partially Collapsed Gibbs (PCG) sampler. In our context, $p(\cdot)$ denotes the target posterior distribution and $\theta = (\sigma_1^2, \sigma_2^2, \sigma_\Delta^2, \epsilon_\gamma, \psi_U, \phi_U, \psi_\Delta, \psi_{\gamma_0}, \psi_{\gamma_1}, \boldsymbol{\beta})^T$. Compared to the ordinary Gibbs sampler, the PCG sampler drops the conditioning on $\mathbf{U}$ when sampling τ and α, and then modifies the order of sampling in the ordinary Gibbs to ensure the stationary distribution of the chain under PCG.

and add $\epsilon_\gamma \sim N(\mathbf{0}, \sigma_\gamma^2)$ to the level 2 prior. The full conditional for $\mathbf{U}$ now involves the covariance matrix $(\sigma_1^2 \mathbf{I}_{MN})^{-1} + \Sigma_U^{-1}$, which can be factored into a Kronecker product of a spatial and a temporal covariance matrix. If the variance decreases after the changepoint, we simply let $\epsilon_1 = \epsilon_2 + \epsilon_\gamma$ where ϵ_γ now is independent with ϵ_2. Then, we replace $\epsilon_\gamma \circ \mathbf{1}_\tau^+$ with $\epsilon_\gamma \circ \mathbf{1}_\tau^-$ and σ_1^2 with σ_2^2 in (10). One caveat of this approach is that we need to pre-specify whether the variance increases or decreases beforehand. We recommend trying both scenarios in parallel and choosing a better model based on Deviance Information Criterion (DIC).

To address the potential challenge of identifiability between $\mathbf{U}$ and $\boldsymbol{\mu}_\tau$ in sampling, we adopt the Partially Collapsed Gibbs (PCG) sampler proposed by Van Dyk and Park [2008], which allows us to remove the conditioning on $\mathbf{U}$ when sampling τ and $\alpha = (\alpha_0, \gamma_0, \gamma_1)^T$. We refer to Van Dyk and Park [2008] and Van Dyk and Jiao [2015] for more details on how to derive the PCG sampler from an ordinary Gibbs sampler. Figure 3 illustrates the sampling procedure for our model under the PCG sampler. It is important to note that, unlike ordinary Gibbs samplers, the order of draws in the PCG sampler must be maintained, as permuting the order may alter the stationary distribution of the chain in the PCG sampler [Van Dyk and Jiao, 2015].

The following discusses the sampling for each parameter in turn. The full conditionals for $\mathbf{U}$ and ϵ_γ are MN-dimensional multivariate normal distributions. To sample $\mathbf{U}$, we leverage the compatibility of a Kronecker product plus a constant diagonal matrix with the eigenvalue decomposition [Stegle et al., 2011], which allows us to sample $\mathbf{U}$ using eigendecompositions of $M \times M$ and $N \times N$ matrices. While the posterior for ϵ_γ is no longer identically distributed, Section 1 of the Supplement [Shi-Jun et al., 2023] shows that its independence structure is still preserved. Thus, posterior samples can be drawn easily even when the spatial and/or temporal dimension is high. See the Supplement Material [Shi-Jun et al., 2023] for more details.

Parameters Δ, γ_{0R}, and γ_{1R} are sampled via a Metropolis Hastings algorithm. While the full conditionals for γ_{0R} and γ_{1R} have closed forms, the resulting distribution involves $MN \times MN$ covariance matrices, making the sampling computationally expensive. To achieve efficient mixing, we employ an adaptive component-wise Metropolis-within-Gibbs [Roberts and Rosenthal, 2009] to propose a new state for each of the N locations separately and automatically tune the acceptance ratios for each location as closely as possible to 0.44, a ratio considered optimal for one-dimensional Gaussian proposals [Roberts and Rosenthal, 2001].

Finally, the parameters $\sigma_U^2, \sigma_1^2, \sigma_2^2, \sigma_\Delta^2, \sigma_{\gamma_0}^2, \sigma_{\gamma_1}^2, \boldsymbol{\beta}$, and $\alpha = (\alpha_0, \gamma_0, \gamma_1)^T$ are assigned conjugate priors and estimated via a Gibbs sampler. We specify weakly independent normal prior for α and $\boldsymbol{\beta}$ and inverse gamma priors for variance parameters $\sigma_1^2, \sigma_2^2, \sigma_U^2$, and σ_Δ^2. For $\sigma_{\gamma_0}^2$ and $\sigma_{\gamma_1}^2$, we use a truncated inverse gamma prior and choose the upper truncation points to be a small fraction of γ_{0F} and γ_{1F}. This encourages the magnitude of random effect to be smaller than that of the fixed effect, which further ensures identifiability. The parameters $\psi_U, \phi_U, \psi_\Delta, \psi_{\gamma_0}, \psi_{\gamma_1}$ are given uniform priors and are sampled via the Metropolis Hastings algorithm. For τ_0, any discrete probability distribution that takes values in $\{1, 2, \ldots, M\}$ can be used as a prior. The full conditional distributions and sampling details are outlined in Section 1 of the Supplement [Shi-Jun et al., 2023].

4   Simulation Study

We perform simulation studies to evaluate the accuracy of our model in detecting and estimating three different types of changes – mean shift only, variance shift only, and mean and variance shift. We compare our method with a univariate time series changepoint detection method derived by only considering $N = 1$ in our model. This univariate method still

considers temporal correlation but no spatial correlation and is applied to each of the spatial locations separately. We also explore how the magnitude of change affects the model's performance.

4.1   Setup

To generate data for simulation, we select $N = 121$ spatial locations on an 11×11 grid and randomly choose one of the grid locations as $\mathbf{s_0}$. The grid is on a surface of a sphere with latitudes from $0°$ to $50°$ and longitudes from $0°$ to $50°$, both in an increment of $5°$. At each location, we consider a time series of length $M = 61$ and generate $\tau(\mathbf{s})$ using (5), with $\tau_0 = 18$, $\boldsymbol{\beta} = (1.5, 1)^T$, $\sigma_\Delta^2 = 1$, and $\psi_\Delta = 0.5$. These values were chosen such that the number of locations with changepoint $|\{\mathbf{s} : \tau(\mathbf{s}) < M\}|$ is comparable to the number of locations without changepoints $|\{\mathbf{s} : \tau(\mathbf{s}) \geq M\}|$ on average. Since a changepoint detection is equivalent to a classification problem, having a balance between the two classes ensures our evaluation focuses on method performance without being affected by class imbalance.

We use model (1) to generate data but replace $\mu_2(\mathbf{s}, t)$ in model (3) by $\mu_2(\mathbf{s}, t) = \alpha_0 + \gamma_0$. This simple version of $\mu_2(\mathbf{s}, t)$ serves the purpose of changepoint detection evaluation and offers a fair comparison with the classic method for which the default model contains no slope after the changepoint. Without loss of generality, we fix the pre-changepoint mean $\alpha_0 = 0$ and variance $\sigma_1^2 = 1$. We let γ_0 take values in $\{0, 1.5, 2, 3\}$ and σ_γ^2 in $\{0, 3, 5\}$ to study the model performance under different strengths of mean and variance shift. The parameters σ_U^2, ϕ_U, and ψ_U are set to 1, 1.5, and 2, respectively, to emulate spatial and temporal dependence observed in real data based on our exploratory data analysis of global surface temperature data. We run 100 simulations for each setting. The ratio of the number of locations without changepoints to those with changepoints in our simulated data ranges from 32:89 to 101:20, with an average of 57:64.

In implementing our method, we assume no prior knowledge about τ_0 and use a discrete uniform prior. This is slightly more challenging than our real problem, since for the Pinatubo data, we know τ_0 is likely right after the eruption. We give weakly informative prior for other unknown parameters. We use the posterior mode of $\min\{M, \tau(\mathbf{s})\}$ as the estimated changepoint for location $\mathbf{s}$. If the mode for $\min\{M, \tau(\mathbf{s})\}$ is at M, we determine that there is no changepoint at $\mathbf{s}$.

To evaluate the performance of our method, we use the metrics of false positive rate (FPR) and false negative rate (FNR) to measure the accuracy of the changepoint detection, and use root mean squared error (RMSE), empirical coverage of the 95% credible interval (CI), and length of the CI to assess the changepoint estimation. FPR is defined as the ratio of the number of falsely detected locations to the total number of locations without changepoints, and FNR is the ratio of the number of falsely undetected locations to the total number of locations with changepoints. When calculating RMSE, we treat the true changepoint as having value M (i.e., $\tau(\mathbf{s}) = M$) when there is no changepoint at location $\mathbf{s}$. A combination of a narrower credible interval with empirical coverage closer to the nominal level indicates a more precise uncertainty quantification. The formula for FPR, FNR, and RMSE are given below, where $\tau(\mathbf{s})$ denotes the true changepoint for location $\mathbf{s}$, $\hat{\tau}(\mathbf{s})$ denotes the detected changepoint, and $|A|$ is the cardinality of set A:

$$FPR = \frac{FP}{FP + TN} = \frac{|\{\mathbf{s} : \hat{\tau}(\mathbf{s}) < M, \tau(\mathbf{s}) = M\}|}{|\{\mathbf{s} : \tau(\mathbf{s}) = M\}|}$$

$$FNR = \frac{FN}{FN + TP} = \frac{|\{\mathbf{s} : \hat{\tau}(\mathbf{s}) = M, \tau(\mathbf{s}) < M\}|}{|\{\mathbf{s} : \tau(\mathbf{s}) < M\}|}$$

$$RMSE = \sqrt{\frac{\sum_{\mathbf{s}} (\tau(\mathbf{s}) - \hat{\tau}(\mathbf{s}))^2}{N}}$$

We compare the FPR, FNR and RMSE of our spatio-temporal model with the univariate method applied to each location (hereinafter 1D method). Through experimentation, we picked a conservatively large iteration number of $20,000$ and a burn-in size of $10,000$ to ensure MCMC convergence based on Gelman-Rubin diagnostic [Gelman and Rubin, 1992].

4.2   Results

Figure 4 summarizes the results for detecting and estimating changepoints only in the mean under different magnitudes of change. Mean shift of zero indicates no changepoint, i.e. $\tau(\mathbf{s}) = M$ for all locations, while a larger mean shift indicates a stronger signal.

The FPR of both methods are comparable when a changepoint is present. Still, our method seems more stable when signal is strong. When there is no changepoint, our method returns a much lower FPR. The FNRs of the two methods are comparable when the signal is strong, but our method largely outperforms the 1D under a weaker signal. Note that FNR is not defined when there is no changepoint. Both the 1D and our method achieve smaller RMSE when the

signal is stronger, but our method outperforms the 1D method across all signal strengths with significantly smaller RMSE. The advantage of our method in terms of RMSE is more pronounced when the signal is weaker. The empirical coverage of the 95% credible intervals obtained from the 1D method appears to be above the nominal level for all tested cases. However, the mean empirical coverage of our method is centered around the nominal level. More importantly, our method results in a much narrower and thus more informative credible interval compared to the 1D method. Unsurprisingly, the length of the credible interval gets wider as the signal becomes weaker. Although there is no simple interpretation for the empirical coverage of Bayesian credible intervals as there is for confidence intervals, our results still suggest a positive view of our credible intervals. The lengths of the credible interval appear to be informative given that the maximum interval length is 60. Unsurprisingly, the length of the credible interval gets wider as the signal becomes weaker.
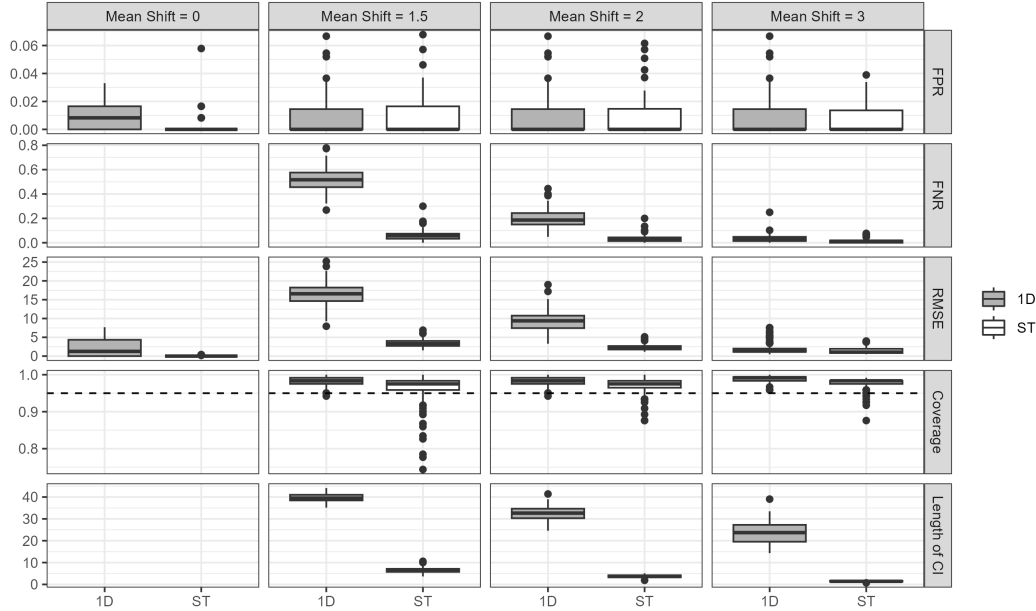

Fig. 4: Boxplots of RMSE, FPR, FNR, the empirical coverage probability and the length of 95% credible intervals under different mean shift signal strength. "ST" is our spatio-temporal model and "1D" is the univariate method. FNR is not defined under Mean Shift=0.

Figure 5 shows the results for both variance shift only and mean and variance shift combined. We show results for $\gamma_0 \in \{0, 2\}$ associated with zero and positive mean shift, and the variance difference parameter $\sigma_\gamma^2 \in \{3, 5\}$, representing two different levels of variance shift. The results for $\gamma_0 \in \{1.5, 3\}$ and $\sigma_\gamma^2 \in \{3, 5\}$ are provided in Section 2 of the Supplement [Shi-Jun et al., 2023].

In the case of variance only shift, our method significantly outperforms the 1D method, with even a wider margin, in all metrics except for FPR. The 1D method appears to be very conservative in detecting variance only shift, resulting in a lower FPR but an extremely high FNR. This implies that the 1D method is less sensitive to variance changes than mean changes.

For combined mean and variance shift, the results seem to be very similar to those for mean shift only. The FPR is comparable for both methods, while the FNR and RMSE are much lower for our method. In this combined case, the empirical coverage of credible intervals for the 1D method is closer to, though still larger than, the nominal level. Once again, the credible intervals obtained from our method are much shorter than the 1D method without sacrificing their empirical coverage.

For each simulation, we calculate the posterior estimate of the parameter by taking posterior mode for τ_0 and posterior mean for all other parameters. To give an example of parameter estimation with our method, we summarize the parameter estimates for the simulations with mean shift of 1.5 and $\sigma_\gamma^2 = 0$ in Table 1. The second and third columns of the table report the mean estimates and the 95% credible intervals across the 100 simulations. We observe that the true value is captured by the 95% interval for all parameters in the model.
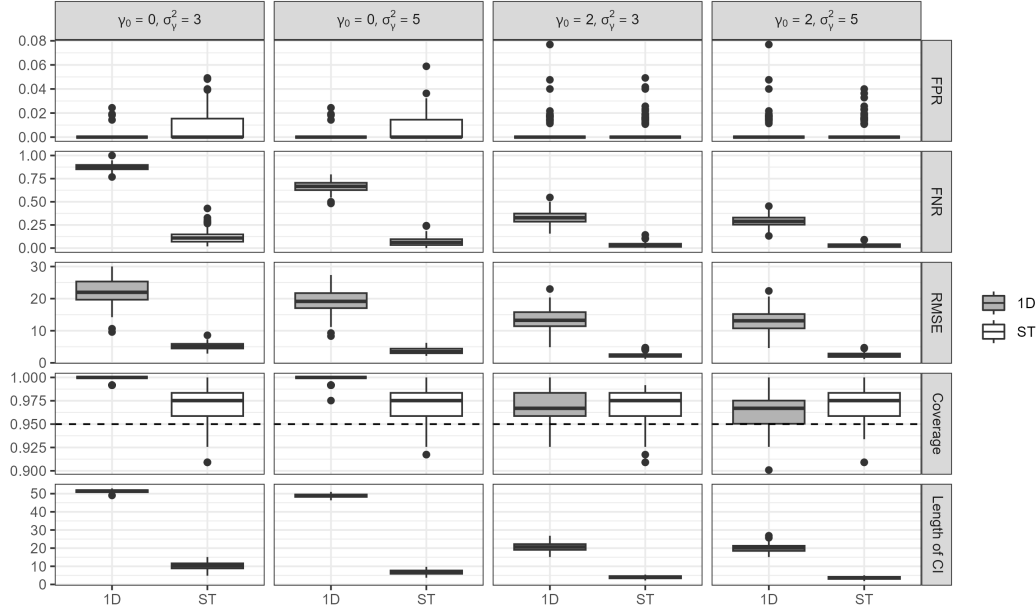
Fig. 5: Boxplots of RMSE, FPR, FNR, the empirical coverage probability and the length of 95% credible intervals under four settings comprised of two γ_0 values representing mean change and two σ_γ^2 values representing variance change. $\gamma_0 = 0$ indicates no mean change. "ST" is our spatio-temporal model and "1D" is the univariate method.

Parameter	True Value	Mean of the estimate	95% CI of the mean
α_0	0	0.0014	(-0.0831, 0.0754)
γ_{0F}	1.5	1.4616	(1.3260, 1.6342)
σ_1^2	1	1.0309	(0.8844, 1.2461)
σ_U^2	1	0.9335	(0.7634, 1.1445)
ψ_U	2	1.8901	(1.5467, 2.3630)
ϕ_U	1.5	1.4489	(1.1393, 1.7735)
τ_0	18	16	(8, 20)
β_1	1.5	1.4366	(0.9382, 2.3505)
β_2	1	1.0408	(0.6369, 1.6172)
σ_Δ^2	1	0.8644	(0.6362, 1.3412)
ψ_Δ	0.5	0.6572	(0.3544, 1.0177)

Table 1: Summary of parameter estimates for a mean shift of 1.5 and variance shift of 0.

Overall, our method outperforms the 1D method by taking advantage of the spatial correlation in the changepoint process for spatially indexed time series. The importance of borrowing strength from neighboring locations becomes more pronounced and necessary when the change signal is weaker. Similar phenomena were observed by Wang et al. [2023].

5   Impact of Mt Pinatubo Volcanic Eruption

We apply our proposed method to AOD and surface temperature data to detect changes that are possibly caused by the aerosols injected into the stratosphere by the Mt. Pinatubo eruption in June 1991. All MCMC convergence in the data analyses have been verified by the Gelman-Rubin diagnostic using three parallel chains with different initial values for the parameters.

	$\sigma_1^2 = \sigma_2^2$	$\sigma_1^2 < \sigma_2^2$	$\sigma_1^2 > \sigma_2^2$	95 % CI for $\sigma_1^2 = \sigma_2^2$
DIC	3,526,069	3,638,721	3,719,177	
α_0	0.2754	0.1913	0.2499	(0.0754,0.4808)
γ_{0F}	4.2408	4.2825	4.923	(3.4503,4.7342)
γ_{1F}	-0.0820	-0.0888	-0.0881	(-0.0996,-0.0646)
σ_U^2	1.1449	1.1391	1.1410	(1.0131,1.3127)
σ_1^2	0.3512	0.2790	0.1409	(0.2563,0.5245)
σ_2^2	NA	0.3092	0.1348	NA
σ_γ^2	NA	0.0302	0.0061	NA
β_1	-0.0186	-0.0092	-0.0151	(-0.1488,0.1020)
β_2	0.5404	0.4447	0.4490	(0.1562,0.9623)
σ_Δ^2	0.9036	0.8288	0.8587	(0.4766,1.786)
ψ_U	2.5679	2.8244	2.6175	(2.0745,2.9091)
ϕ_U	0.8336	0.8965	0.8229	(0.7161,0.9198)
ψ_Δ	0.8084	0.8489	0.8212	(0.3817,1.7390)
$\sigma_{\gamma_0}^2$	1.5794	1.3702	1.7418	(1.0757,2.1393)
$\sigma_{\gamma_1}^2$	0.0006	0.0007	0.0007	(0.0004,0.0011)
ψ_{γ_0}	6.7958	7.5673	5.8663	(4.1403,10.7769)
ψ_{γ_1}	6.5380	5.9436	5.8552	(4.3915,9.9309)

Table 2: DIC values and posterior summary of parameters under different model assumptions for AOD data. The credible intervals in the last column are derived under $\sigma_1^2 = \sigma_2^2$.

5.1 Aerosol Optical Depth

Following the suggestions in Section 3.2, we apply model (1) on the aerosol data with both $\sigma_1^2 < \sigma_2^2$ and $\sigma_1^2 > \sigma_2^2$ since we have no prior knowledge about whether the variance increases or decreases after changepoint. In addition, we also test the case of $\sigma_1^2 = \sigma_2^2$, which means that the change is solely due to a mean shift.

We set $\mathbf{s}_0$ to be at (123.4375°E, 19°N), the center of the grid cell that contains the location of Mt. Pinatubo (120°E, 15°N). We anticipate $\mathbf{s}_0$ has the earliest changepoints among all grid points. We use a discrete uniform prior for τ_0 and weakly informative priors for all other parameters. Table 2 compares the DIC value and the posterior mean of key parameter estimates for the three forms of variance shift models. We observe that the equal variance model achieves the lowest DIC value. Consistent with this finding, the estimated variance shift parameter σ_γ^2 for the variance increase or decrease assumptions is very small compared to σ_1^2 or σ_2^2. Thus, we proceed with our inference based on the assumption $\sigma_1^2 = \sigma_2^2$, that is, the change is only due to a mean shift.

We report the 95% credible intervals of key parameters under the assumption of $\sigma_1^2 = \sigma_2^2$ in Table 2. The significantly positive estimate of γ_{0F} indicates an elevated aerosol level immdediately after the volcanic eruption, and the negative estimate of γ_{1F} indicates the subsequent restoration of aerosol level post-eruption, consistent with the anticipated trend. The diffusion parameter for longitude, β_1, is not significantly different from 0. In contrast, there is strong evidence to show that the diffusion parameter for latitude, β_2, is substantially greater than 0. This observation aligns with the spatial pattern of changepoints predominantly driven by latitude, as depicted in Figure 2(a).

We determine the estimated changepoints by taking the posterior mode of the floor function of $\min\{M, \tau(\mathbf{s})\}$ at each location. Figure 6(a) shows the heatmap of estimated changepoints. Our model detects a changepoint at all locations, with estimated values ranging from Jun 1991 to Sep 1991. The estimated changepoints show a pattern driven more by latitude than longitude, with the earliest changepoints predominantly occurring along latitudes 3.5°S through 34°N. This pattern aligns with our exploratory data analysis and is consistent with existing literature, which reports that the Pinatubo aerosol layer circled the Earth in 21 days and had spread to latitudes around 30°N and 10°S in the same period [Self et al., 1996]. McCormick and Veiga [1992] and Stowe et al. [1992] also found the Pinatubo aerosols straddled the equator. Figure 6(b) displays the estimated mean shift parameter, $\gamma_0(\mathbf{s})$, which ranges from +0.25 to +1.5. The spatial pattern of the estimated mean change matches with that shown in Figure 2(b), indicating the successful capture of the spatial variability in mean change by our method.

The time series of AOD after preprocessing and the estimated μ_1 and $\mu_2(\mathbf{s}, t)$ from our model are shown in Figure 7. Our mean estimates follow the same pattern as the preprocessed data, of which the time series close to the equator in the latitude bands $20°S - 20°N$ jump first and tend to have a higher peak compared to those around the latitudes further north or south. These results, together with Figure 6, demonstrate that our model effectively captures the diffusion of the

impact of the volcanic eruption on AOD. Specifically, the estimated changepoints for locations near the latitude of Mt. Pinatubo (15°N) coincide with the month of the eruption, while the changepoints for locations further north or south occur several months later. We also plot the residuals for the AOD series by location in Section 2 of the Supplement [Shi-Jun et al., 2023], which verifies that $\sigma_1^2 = \sigma_2^2$ is a reasonable assumption.
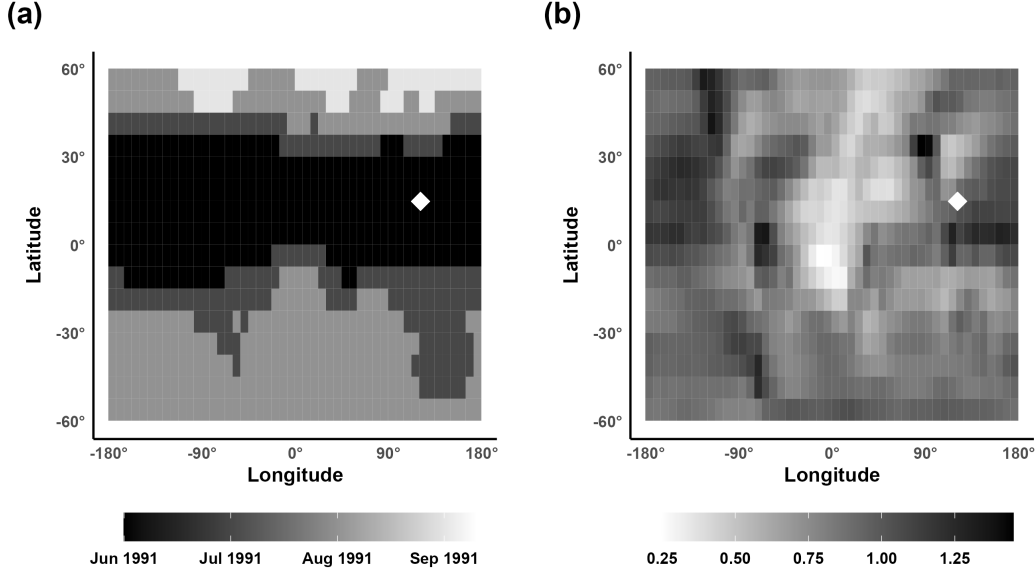

Fig. 6: (a) Heatmap of detected changepoints for AOD. Darker color indicates earlier change. (b) Heatmap of estimated change amount. Darker color indicates larger magnitude of change. The white diamond marks the location of Mt. Pinatubo.
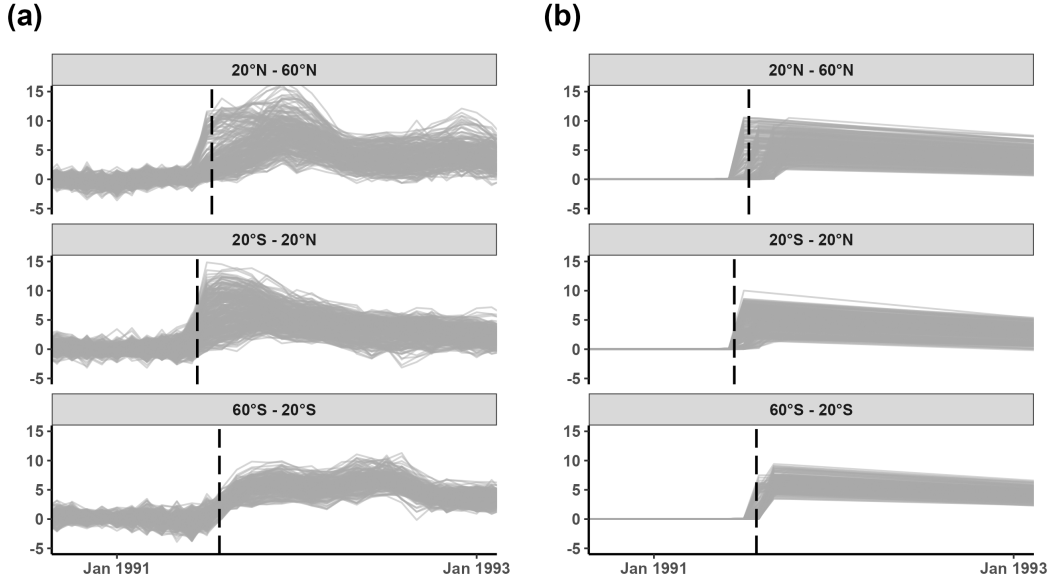

Fig. 7: Time series of (a) AOD after preprocessing and (b) posterior mean of μ_1 and $\mu_2(\mathbf{s}, t)$, zoomed in to years $1991 - 1993$. The dashed line marks the average value of the changepoints in latitude bands $(60°S - 20°S)$, $(20°S - 20°N)$, and $(20°N - 60°N)$.

	$\sigma_1^2 = \sigma_2^2$	$\sigma_1^2 < \sigma_2^2$	$\sigma_1^2 > \sigma_2^2$	95% CI
DIC	-1,692	-1,543	-1,631	for $\sigma_1^2 = \sigma_2^2$
α_0	0.2092	0.2117	0.2103	(0.1182,0.3074)
γ_{0F}	-0.8440	-0.8592	-0.8430	(-1.1714,-0.5410)
γ_{1F}	-0.0117	-0.0116	-0.0116	(-0.0213,-0.0028)
σ_U^2	0.7918	0.7933	0.7901	(0.7242,0.8655)
σ_1^2	0.1029	0.1046	0.1068	(0.0798,0.1436)
σ_2^2	NA	0.1127	0.1011	NA
σ_γ^2	NA	0.0081	0.0057	NA
σ_Δ^2	20.16	20.92	20.43	(8.33,56.65)
ψ_U	4.9675	4.8348	4.8779	(4.2658,5.6670)
ϕ_U	1.2129	1.2063	1.1958	(1.0662,1.3851)
ψ_Δ	1.7805	2.0915	1.8195	(0.8843,3.0968)
$\sigma_{\gamma_0}^2$	0.0390	0.03870	0.0312	(0.0145,0.1516)
$\sigma_{\gamma_1}^2$	3.49e-5	3.63e-5	3.56e-5	(1.93e-6,9.88e-5)
ψ_{γ_0}	21.46	20.63	23.38	(15.29,28.47)
ψ_{γ_1}	27.48	25.75	25.51	(18.50,28.66)

Table 3: DIC values and posterior summary of parameters under different model assumptions for surface temperature data. The credible intervals in the last column are derived under $\sigma_1^2 = \sigma_2^2$.

5.2 Zonal surface temperature data

Unlike the clear signal of volcanic impact on stratospheric AOD data, the impact on surface temperature is visually indiscernible, as observed in Figure 1. Indeed, the impact was too subtle to be detected when we applied our method to the gridded temperature data as was done for AOD data. Due to the strong latitudinal, or zonal, trend of AOD, the impact of volcanic eruption on surface temperature is not as local as the observed impact on AOD. Changes in surface temperature following the eruption are more noticeable when aggregated by zonal bands, as mentioned in Section 2. Consequently, we use zonal mean temperatures to trace the impact of the eruption. The mechanism behind how aerosols ejected into the lower stratosphere affect surface temperature is a complex process. Unlike AOD, we do not expect the volcanic impact on surface temperatures to diffuse from the event location [Robock and Matson, 1983]. Thus, we negate the influence of the distance from $\mathbf{s_0}$ on $\tau_0(\mathbf{s})$ by setting $\beta = 0$ in the mean of $\log(\mathbf{\Delta})$. For this data, $\mathbf{s_0}$ is interpreted as the location corresponding to the smallest $\tau(\mathbf{s})$ estimate.

Previous literature has found that the effect of the Mt. Pinatubo eruption on surface temperature mostly took place in the two-year period following the eruption [Robock and Matson, 1983, Self et al., 1996]. Therefore, we give τ_0 an equal weight discrete uniform prior covering the months in the following two years and the last month in the data: $\{1991/06, 1991/07, \ldots 1993/06, 1995/12\}$. The last time point, 1995/12, indicates the possibility that there is no observed changepoint at any of the locations.

Similar to the AOD data, we apply Model (1) with $\sigma_1^2 < \sigma_2^2$, $\sigma_1^2 > \sigma_2^2$, and $\sigma_1^2 = \sigma_2^2$ to surface temperature and compare the results of the three models in Table 3. Again, the mean shift only model ($\sigma_1^2 = \sigma_2^2$) achieves the lowest DIC, and the estimated variance change parameter σ_γ^2 for the two variance shift models is very small compared to σ_1^2 or σ_2^2. We thus proceed with our analysis under the assumption $\sigma_1^2 = \sigma_2^2$. Table 3 reports the posterior mean and the 95% credible interval of key parameters. Unlike the AOD data, the mean shift parameter γ_{0F} for temperature is significantly negative, indicating the global cooling effect of eruption consistent with other literature. The slope parameter γ_{1F} is also significantly negative, indicating continued cooling of the global temperature after the changepoint during the time period considered in our data.

Figure 8 shows the posterior mean of μ_1 and $\mu_2(\mathbf{s}, t)$ for the temperature series at each latitude, separated at the posterior mode of $\tau(\mathbf{s})$. Our method detects changepoints for all latitudes in the range $(56°S - 49°N)$ except for latitudes $18.5°S, 26.5°N$, and $34.0°N$. No changepoints were detected in the southern $(86°S - 63.5°S)$ and northern $(56.5°N - 86.5°N)$ ends of the globe. The posterior probability of having no changepoint ranges from 0 to 0.0112 for the detected latitudes and 0.7955 to 0.9986 for the undetected latitudes. The detected changepoints range from Sep 1991 - May 1992. See Table 1 in the Supplement [Shi-Jun et al., 2023] for further details. The lack of changepoint in the latitudes $18.5°S, 26.5°N, 34.0°N$ may potentially be due to low signal-to-noise ratio in the subtropics (roughly $23°$ to $35°$ north and south) which are particulary synoptically active [McClain et al., 2004, Ryoo et al., 2008, Lensky et al., 2018]. As shown in Figure 8, at all these three latitudes, we observe a noticeable drop in the temperature shortly
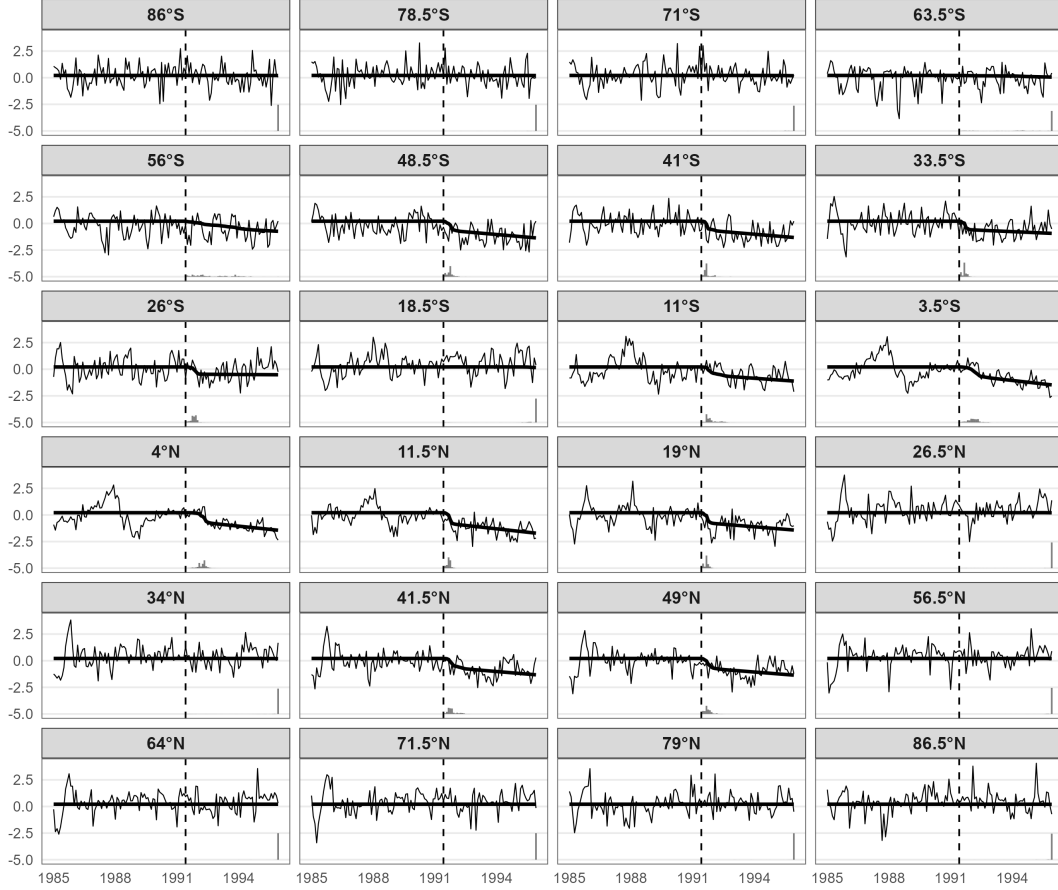
Fig. 8: Posterior mean of μ_1 and $\mu_2(\mathbf{s}, t)$ for surface temperature, separated at the posterior mode of $\tau(\mathbf{s})$ (thick black lines). The thin black lines are latitudinal mean temperature series after preprocessing. The posterior distribution of the changepoints are overlayed at the bottom of each plot. No changepoints were detected at 86.0°S - 63.5°S, 18.5°S, 26.5°N, 34.0°N, and 56.5°N - 86.5°N. The dashed vertical lines mark the month of the eruption (1991/06)

after the Pinatubo eruption but then immediately followed by a rise, likely due to the volatile nature of subtropics. The few data points in the temperature drop make the changepoint detection very challenging as they simply behave like noise. In conclusion, we cannot assert that these three latitudes were not affected by the Mt. Pinatubo eruption, but the fingerprint of the eruption on those latitudes (if any) is brief and weak that can be easily masked by the natural fluctuation, based on the MERRA-2 data we used in our analyses.

The magnitude of the mean shift shown in Figure 8 is not true to scale since we normalized the data to make the variance constant for all locations in the preprocessing step. Figure 9 shows the posterior distribution of the actual mean shift at the detected latitudes, after back-transforming to match the scale of the original data. While there were more changepoints detected in the southern hemisphere, the magnitude of change is smaller compared to the northern hemisphere, and the change in global temperature is mostly driven by the latitudes $41.5°N$ and $49°N$. The average mean change in the southern hemisphere, northern hemisphere, and the globe is $-0.136°C$, $-0.205°C$, and $-0.191°C$, respectively. Our findings are consistent with the existing studies [Self et al., 1996], which report that the Mt. Pinatubo eruption led to a global cooling of $0.4°C$ between years 1991 and 1993, driven mostly by a cooling of $0.5°C$ in Northern Hemisphere. The estimated change amounts by our model are smaller in magnitude, which is expected since our method only measures the amount of mean shift at the time of the changepoint as opposed to the average change over two years. The negative γ_{1F} estimate also indicates that the temperature continues to cool down after the changepoint.

Our findings from the analysis of stratospheric AOD and surface temperature data are consistent with the previous studies in general. However, our work complements the previous studies by providing quantitative regional measures of the impact of the Pinatubo eruption on aerosol and climate, as well as specifying the spatial pattern of the impact.
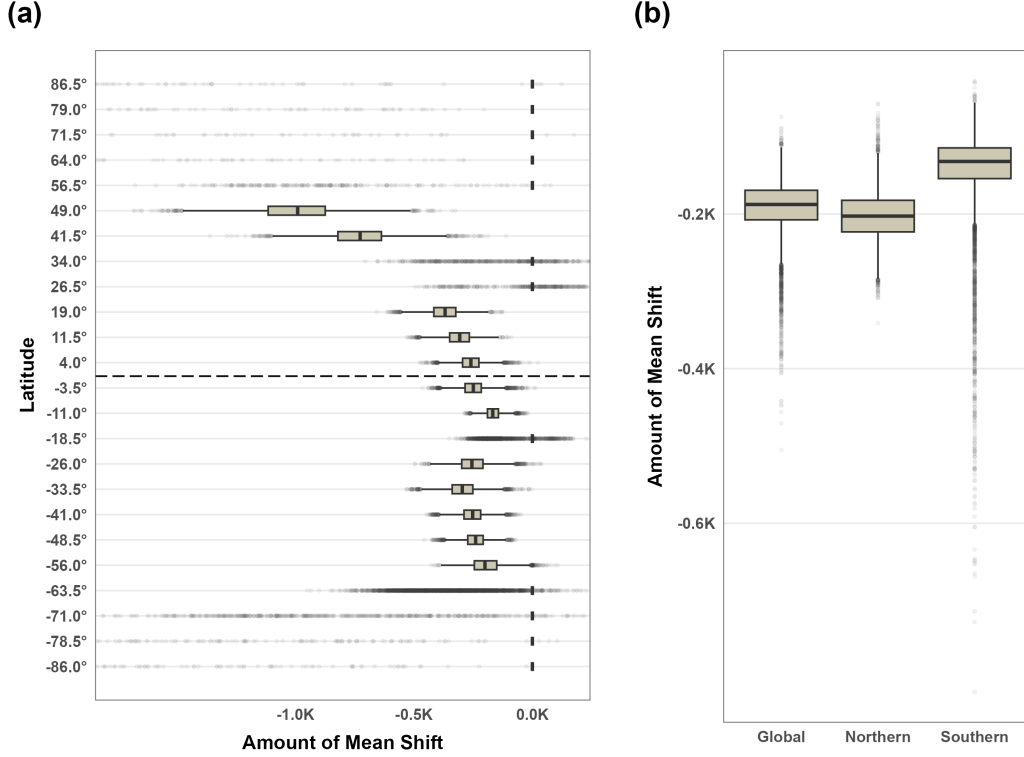
14

Fig. 9: Posterior distribution of $\gamma_0(\mathbf{s})$ (a) by latitude and (b) averaged over hemisphere after backtransforming to the original scale of surface temperature data. The dashed line in (a) marks the equator.

6 Discussion

Motivated by the need to quantify the impact of the Mt. Pinatubo eruption on regional climate and specify its spatial pattern, we proposed a Bayesian framework to simultaneously detect and estimate changepoint for spatio-temporal data. Our approach can identify which spatial locations have a changepoint and, meantime, allows the changepoints and the magnitude of change to vary spatially, as opposed to assuming that all locations experience the same amount of change at the same time point. Furthermore, our model respects the diffusion pattern of the impact of the volcanic eruption and takes advantage of spatial correlation in changepoint detection and estimation. In particular, our method ensures that changepoints at locations other than the event origin occur strictly after the initial changepoint. This feature helps to prevent detecting changepoints caused by unrelated events, providing a more focused analysis of the targeted atmospheric event. The validity and effectiveness of our approach are demonstrated through simulations. By applying our method to AOD and surface temperature data, we successfully captured the spatial patterns of changepoints, which reveals the progression of injected aerosol and its spatially heterogeneous impact on regional aerosol optical depth and surface temperatures.

For convenience, we have opted for the exponential covariance function, a stationary model, to address spatial correlation in the data. However, given our large spatial domain, it may be more realistic to consider a nonstationary covariance function, such as those proposed by Shand and Li [2017]. Other possible improvements of covariance models include employing a chordal of circular Matérn covariance function instead of an exponential covariance model [Guinness and Fuentes, 2016], and a more flexible nonseparable or even asymmetric space-time covariance model [Gneiting, 2002] for $U(\mathbf{s}, t)$. Another interesting extension of our work is to directly consider a bivariate time series of AOD and surface temperature in changepoint detection and estimation. This may especially benefit the surface temperature due to the weaker signal in temperature than in AOD. This extension is expected to be involving, though, as the dependency structure of the bivariate data will be complex, and the changepoint processes for the two variables will also interact with each other. Additionally, our current method focuses on detecting the time at which the impact of the eruption first reaches each location. Capturing the whole life process of Pinatubo impact including when the data "returns to normal" will be an exciting but nontrial extention of our current method as that requires estimation of more than one changepoint at each location, aligning with the concept of "epidemic changepoints" [Tucker and Yarger, 2023].

Finally, we by no means imply a causal relationship between the Mt. Pinatubo eruption and the detected changepoints. These changepoints could be due to other climate and weather events, such as the El Niño effect, or other internal variations. Our aim in this article is to capture a plausible impact of the Mt. Pinatubo volcanic eruption. Separating Mt. Pinatubo's impact from other scenarios and establishing a pure causal relationship between the volcanic eruption and climate impact is nontrivial and is a topic we reserve for future studies.

Acknowledgments

References

Stephen Self, Jing-Xia Zhao, Rick E. Holasek, Ronnie C. Torres, and Alan J. King. chapter The atmospheric impact of the 1991 Mount Pinatubo eruption, pages 1089–1115. University Washington Press, 1996.

Alan Robock. Stratospheric aerosol geoengineering. *Issues in Environmental Science and Technology*, 2014:162–185, 01 2014. doi: 10.1063/1.4916181.

Georgiy Stenchikov, Thomas L. Delworth, V. Ramaswamy, Ronald J. Stouffer, Andrew Wittenberg, and Fanrong Zeng. Volcanic signals in oceans. *Journal of Geophysical Research: Atmospheres*, 114(D16), 2009. doi: https://doi.org/10.1029/2008JD011673. URL https://agupubs.onlinelibrary.wiley.com/doi/abs/10.1029/2008JD011673.

K. Labitzke and M. P. McCormick. Stratospheric temperature increases due to pinatubo aerosols. *Geophysical Research Letters*, 19(2):207–210, 1992. doi: https://doi.org/10.1029/91GL02940. URL https://agupubs.onlinelibrary.wiley.com/doi/abs/10.1029/91GL02940.

Ellsworth G. Dutton and John R. Christy. Solar radiative forcing at selected locations and evidence for global lower tropospheric cooling following the eruptions of el chichón and pinatubo. *Geophysical Research Letters*, 19(23):2313–2316, 1992. doi: https://doi.org/10.1029/92GL02495. URL https://agupubs.onlinelibrary.wiley.com/doi/abs/10.1029/92GL02495.

David W. J. Thompson, John M. Wallace, Phil D. Jones, and John J. Kennedy. Identifying signatures of natural climate variability in time series of global-mean surface temperature: Methodology and insights. *Journal of Climate*, 22(22): 6120 – 6141, 2009. doi: https://doi.org/10.1175/2009JCLI3089.1. URL https://journals.ametsoc.org/view/journals/clim/22/22/2009jcli3089.1.xml.

Dennis W Hallema, Ge Sun, Peter V Caldwell, Steven P Norman, Erika C Cohen, Yongqiang Liu, Eric J Ward, and Steven G McNulty. Assessment of wildland fire impacts on watershed annual water yield: Analytical framework and case studies in the united states. *Ecohydrology*, 10(2):e1794, 2017.

Michael W Robbins, Robert B Lund, Colin M Gallagher, and QiQi Lu. Changepoints in the north atlantic tropical cyclone record. *Journal of the American Statistical Association*, 106(493):89–99, 2011.

J Derek Tucker and Drew Yarger. Elastic functional changepoint detection of climate impacts from localized sources. *Environmetrics*, page e2826, 2023.

Jaxk Reeves, Jien Chen, Xiaolan L Wang, Robert Lund, and Qi Qi Lu. A review and comparison of changepoint detection techniques for climate data. *Journal of Applied Meteorology and Climatology*, 46(6):900–915, 2007.

Samaneh Aminikhanghahi and Diane J Cook. A survey of methods for time series change point detection. *Knowledge and Information Systems*, 51(2):339–367, 2017.

Rebecca Killick, Paul Fearnhead, and Idris A Eckley. Optimal detection of changepoints with a linear computational cost. *Journal of the American Statistical Association*, 107(500):1590–1598, 2012.

Daniel Barry and John A Hartigan. Product partition models for change point problems. *The Annals of Statistics*, pages 260–279, 1992.

Anandamayee Majumdar, Alan E Gelfand, and Sudipto Banerjee. Spatio-temporal change-point modeling. *Journal of Statistical Planning and Inference*, 130(1-2):149–166, 2005.

Xiang Xuan and Kevin Murphy. Modeling changing dependency structure in multivariate time series. In *Proceedings of the 24th International Conference on Machine Learning*, pages 1055–1062, 2007.

Samuel I Berchuck, Jean-Claude Mwanza, and Joshua L Warren. A spatially varying change points model for monitoring glaucoma progression using visual field data. *Spatial Statistics*, 30:1–26, 2019.

Mengchen Wang, Trevor Harris, and Bo Li. Asynchronous changepoint estimation for spatially correlated functional time series. *Journal of Agricultural, Biological and Environmental Statistics*, 28(1):157–176, 2023.

Global Modeling and Assimilation Office (GMAO). Merra-2 tavg1_2d_aer_nx: 2d, 1-hourly, time-averaged, single-level, assimilation, aerosol diagnostics v5.12.4, 2015a. DOI:10.5067/KLICLTZ8EM9D.

Global Modeling and Assimilation Office (GMAO). Merra-2 tavg1_2d_slv_nx: 2d, 1-hourly, time-averaged, single-level, assimilation, single-level diagnostics v5.12.4, 2015b. DOI: 10.5067/VJAFPLI1CSIV.

RB Cleveland. Stl: A seasonal-trend decomposition procedure based on loess. *Journal of Official Statistics*, 6:3–73, 1990.

Alan Robock and Jianping Mao. The volcanic signal in surface temperature observations. *Journal of Climate*, 8(5): 1086–1103, 1995.

Georgiy Stenchikov, Alan Robock, V Ramaswamy, M Daniel Schwarzkopf, Kevin Hamilton, and S Ramachandran. Arctic oscillation response to the 1991 mount pinatubo eruption: Effects of volcanic aerosols and ozone depletion. *Journal of Geophysical Research: Atmospheres*, 107(D24):ACL–28, 2002.

Chaochao Gao, Alan Robock, and Caspar Ammann. Volcanic forcing of climate over the past 1500 years: An improved ice core-based index for climate models. *Journal of Geophysical Research: Atmospheres*, 113(D23), 2008.

Alan Robock and Michael Matson. Circumglobal transport of the el chichón volcanic dust cloud. *Science*, 221(4606): 195–197, 1983.

Tilmann Gneiting. Strictly and non-strictly positive definite functions on spheres. 2013.

Chunfeng Huang, Haimeng Zhang, and Scott M Robeson. On the validity of commonly used covariance and variogram functions on the sphere. *Mathematical Geosciences*, 43:721–733, 2011.

Samantha Shi-Jun, Lyndsay Shand, and Bo Li. Supplement to "tracing the impacts of mount pinatubo eruption on regional climate using spatially-varying changepoint detection", 2023.

Oliver Stegle, Christoph Lippert, Joris Mooij, Neil Lawrence, and Karsten Borgwardt. Efficient inference in matrix-variate gaussian models with iid observation noise. *Advances in Neural Information Processing Systems*, 24, 2011.

David A Van Dyk and Taeyoung Park. Partially collapsed gibbs samplers: Theory and methods. *Journal of the American Statistical Association*, 103(482):790–796, 2008.

David A Van Dyk and Xiyun Jiao. Metropolis-hastings within partially collapsed gibbs samplers. *Journal of Computational and Graphical Statistics*, 24(2):301–327, 2015.

Gareth O. Roberts and Jeffrey S. Rosenthal. Examples of adaptive mcmc. *Journal of Computational and Graphical Statistics*, 18(2):349–367, 2009.

Gareth O Roberts and Jeffrey S Rosenthal. Optimal scaling for various metropolis-hastings algorithms. *Statistical Science*, 16(4):351–367, 2001.

Andrew Gelman and Donald B Rubin. Inference from iterative simulation using multiple sequences. *Statistical Science*, 7(4):457–472, 1992.

MPs McCormick and RE Veiga. Sage ii measurements of early pinatubo aerosols. *Geophysical Research Letters*, 19(2): 155–158, 1992.

LL Stowe, RM Carey, and PP Pellegrino. Monitoring the mt. pinatubo aerosol layer with noaa/11 avhrr data. *Geophysical Research Letters*, 19(2):159–162, 1992.

Charles R McClain, Sergio R Signorini, and James R Christian. Subtropical gyre variability observed by ocean-color satellites. *Deep Sea Research Part II: Topical Studies in Oceanography*, 51(1-3):281–301, 2004.

J.M. Ryoo, D.W. Waugh, and Andrew Gettelman. Variability of subtropical upper tropospheric humidity. *Atmospheric Chemistry and Physics*, 8(10):2643–2655, 2008.

Itamar M Lensky, Uri Dayan, and David Helman. Synoptic circulation impact on the near-surface temperature difference outweighs that of the seasonal signal in the eastern mediterranean. *Journal of Geophysical Research: Atmospheres*, 123(20):11–333, 2018.

Lyndsay Shand and Bo Li. Modeling nonstationarity in space and time. *Biometrics*, 73(3):759–768, 2017.

Joseph Guinness and Montserrat Fuentes. Isotropic covariance functions on spheres: Some properties and modeling considerations. *Journal of Multivariate Analysis*, 143:143–152, 2016.

Tilmann Gneiting. Nonseparable, stationary covariance functions for space–time data. *Journal of the American Statistical Association*, 97(458):590–600, 2002.

A Supplement to "Tracing the impacts of Mount Pinatubo eruption on regional climate using spatially-varying changepoint detection"

A.1 MCMC sampling

We write the μ_τ as

$$\mu_\tau = \mu_F + \mu_R \circ \mathbf{1}_\tau^+$$
$$= \mathbf{Z}_\tau \alpha + \mu_R \circ \mathbf{1}_\tau^+$$

where $\mu_R = \gamma_{0R} + \gamma_{1R} \cdot (t \otimes \mathbf{1_N} - \mathbf{1_M} \otimes \tau)$, $\mathbf{Z}_\tau = \begin{bmatrix} \mathbf{1_{MN}} & \mathbf{1}_\tau^+ & (t \otimes \mathbf{1}_N - \mathbf{1}_M \otimes \tau) \circ \mathbf{1}_\tau^+ \end{bmatrix}$, and each component of $\alpha = \begin{bmatrix} \alpha_0 & \gamma_0 & \gamma_1 \end{bmatrix}^T$ represents the pre-changepoint mean, amount of mean shift, and post-changepoint temporal trend, respectively.

Step 1 : Sample μ_τ without conditioning on $\mathbf{U}$.

(i) Given prior $\alpha \sim N(0, s_a^2 I_3)$, the full conditional for α with $\mathbf{U}$ integrated out is

$$\alpha \mid \mathbf{Y}, \tau, \mu_R, \theta \sim N(\mu_\alpha, \Sigma_\alpha),$$

where

$$\Sigma_\alpha = \left(\mathbf{Z}^T (\sigma_1^2 \mathbf{I}_{MN} + \Sigma_U)^{-1} \mathbf{Z} + \frac{\mathbf{I}_3}{s_a^2} \right)^{-1},$$
$$\mu_\alpha = \Sigma_\alpha \mathbf{Z}^T (\sigma_1^2 \mathbf{I}_{MN} + \Sigma_U)^{-1} (\mathbf{Y} - (\epsilon_\gamma + \mu_R) \circ \mathbf{1}_\tau^+).$$

(ii) Given prior $\tau_0 \sim Cat(\pi = (\pi_1, \pi_2, \ldots, \pi_M))$, the full conditional for τ_0 with $\mathbf{U}$ integrated out is

$$\tau_0 \mid \mathbf{Y}, \mu_\tau, \tau, \theta \sim Cat(\widetilde{\pi} = (\widetilde{\pi}_1, \ldots, \widetilde{\pi}_M)),$$

where

$$\log \widetilde{\pi}_k \propto -\frac{1}{2} (\mathbf{Z}_\tau \alpha + (\epsilon_\gamma + \mu_R) \circ \mathbf{1}_\tau^+)^T (\sigma_1^2 \mathbf{I}_{MN} + \Sigma_U)^{-1} (\mathbf{Z}_\tau \alpha + (\epsilon_\gamma + \mu_R) \circ \mathbf{1}_\tau^+).$$

(iii) See section A.1.1 on how to sample Δ and μ_R

Step 2 : Sample $\mathbf{U}$.

(i) The full conditional for $\mathbf{U}$ is

$$\mathbf{U} \mid \cdot \sim N(\widetilde{\mu}_U, \widetilde{\Sigma}_U),$$

where

$$\widetilde{\Sigma}_U = \frac{\mathbf{I}_{MN}}{\sigma_1^2} + \Sigma_U^{-1},$$
$$\widetilde{\mu}_U = \widetilde{\Sigma}_U^{-1} \left(\frac{\mathbf{Y} - \mathbf{Z}_\tau \alpha - (\epsilon_\gamma + \mu_R) \circ \mathbf{1}_\tau^+}{\sigma_1^2} \right).$$

Step 3 : Sample θ.

(i) Given priors $\sigma_1^2 \sim IG(a_1, b_1), \sigma_\gamma^2 \sim IG(a_2, b_2), \sigma_U^2 \sim IG(a_3, b_3), \sigma_\Delta^2 \sim IG(a_4, b_4)$, the full conditionals are

$$\sigma_1^2 \mid \cdot \sim IG \left(a_1 + \frac{MN}{2}, b_1 + \frac{(\mathbf{Y} - \mathbf{U} - \mu_\tau - \epsilon_\gamma \circ \mathbf{1}_\tau^+)^T (\mathbf{Y} - \mathbf{U} - \mu_\tau - \epsilon_\gamma \circ \mathbf{1}_\tau^+)}{2} \right)$$

$$\sigma_\gamma^2 \mid \cdot \sim IG \left(a_2 + \frac{K}{2}, b_2 + \frac{\epsilon_\gamma^T \epsilon_\gamma}{2} \right)$$

$$\sigma_U^2 \mid \cdot \sim IG \left(a_3 + \frac{MN}{2}, b_3 + \frac{\mathbf{U}^T \mathbf{R}(\phi_U)^{-1} \otimes \mathbf{R}(\psi_U)^{-1} \mathbf{U}}{2} \right)$$

$$\sigma_\Delta^2 \mid \cdot \sim IG \left(a_4 + \frac{N}{2}, b_4 + \frac{1}{2} (\log \Delta - \mathbf{X}\beta)^T \mathbf{R}(\psi_\Delta)^{-1} (\log \Delta - \mathbf{X}\beta) \right)$$

where K = number of post-cp indices.

19

(ii) Given $\sigma^2_{\gamma_i} \mid \gamma_{iF} \sim TruncIG(\min = 0, \max = \gamma^2_{iF}/9, a_5, b_5), \quad i \in \{0, 1\}$, the full conditionals are

$$\sigma^2_{\gamma_0} \mid \cdot \sim TruncIG\left(\min = 0, \max = \frac{\gamma^2_{0F}}{9}, a_5 + \frac{N}{2}, b_5 + \frac{\boldsymbol{\gamma_{0R}}^T \mathbf{R}(\psi_{\gamma_{0R}})^{-1} \boldsymbol{\gamma_{0R}}}{2}\right)$$

$$\sigma^2_{\gamma_1} \mid \cdot \sim TruncIG\left(\min = 0, \max = \frac{\gamma^2_{1F}}{9}, a_5 + \frac{N}{2}, b_5 + \frac{\boldsymbol{\gamma_{1R}}^T \mathbf{R}(\psi_{\gamma_{1R}})^{-1} \boldsymbol{\gamma_{1R}}}{2}\right)$$

(iii) Given prior $\boldsymbol{\beta} \sim N(\mathbf{0}, s_b^2 \mathbf{I}_2)$, the full conditional for $\boldsymbol{\beta}$ is

$$\boldsymbol{\beta} \sim N(\boldsymbol{\mu_\beta}, \boldsymbol{\Sigma_\beta}),$$

where

$$\boldsymbol{\Sigma_\beta} = \left(\frac{\mathbf{X}^T \mathbf{R}(\psi_\Delta)^{-1} \mathbf{X}}{\sigma^2_\Delta} + \frac{\mathbf{I}_2}{s_b^2}\right)^{-1},$$

$$\boldsymbol{\mu_\beta} = \boldsymbol{\Sigma_\beta}\left(\frac{\mathbf{X}^T \mathbf{R}(\psi_\Delta)^{-1} \log \boldsymbol{\Delta}}{\sigma^2_\Delta}\right).$$

(iv) The full conditional for $\boldsymbol{\epsilon_\gamma}$ is

$$\boldsymbol{\epsilon_\gamma} \sim N(\widetilde{\boldsymbol{\mu}}_\gamma, \widetilde{\boldsymbol{\Sigma}}_\gamma),$$

where

$$\widetilde{\boldsymbol{\Sigma}}_\gamma = diag\left(\left(\frac{\mathbf{1}^+_\tau}{\sigma^2_1} + \frac{\mathbf{1}}{\sigma^2_\gamma}\right)^{-1}\right),$$

$$\widetilde{\boldsymbol{\mu}}_\gamma = \widetilde{\boldsymbol{\Sigma}}_\gamma\left(\frac{Y - \mu_\tau - U}{\sigma^2_1}\right) \circ \mathbf{1}^+_\tau.$$

(v) Given priors $\phi_U \sim Unif(l_1, u_1), \psi_U \sim Unif(l_2, u_2), \psi_\Delta \sim Unif(l_3, u_3)$, the full conditionals are

$$f(\phi_U \mid \cdot) \propto |\mathbf{R}(\phi_U)|^{-N/2} \exp\left(-\frac{\mathbf{U}^T (\mathbf{R}(\phi_U)^{-1} \otimes \mathbf{R}(\psi_U)^{-1}) \mathbf{U}}{2\sigma^2_U}\right) \mathbb{1}(l_1 < \phi_U < u_1)$$

$$f(\psi_U \mid \cdot) \propto |\mathbf{R}(\psi_U)|^{-M/2} \exp\left(-\frac{\mathbf{U}^T (\mathbf{R}(\phi_U)^{-1} \otimes \mathbf{R}(\psi_U)^{-1}) \mathbf{U}}{2\sigma^2_U}\right) \mathbb{1}(l_2 < \psi_U < u_2)$$

$$f(\psi_\Delta \mid \cdot) \propto |\mathbf{R}(\psi_\Delta)|^{-1/2} \exp\left(-\frac{(\log \boldsymbol{\Delta} - \mathbf{X}\boldsymbol{\beta})^T \mathbf{R}(\psi_\Delta)^{-1} (\log \boldsymbol{\Delta} - \mathbf{X}\boldsymbol{\beta})}{2\sigma^2_\Delta}\right)$$
$$\cdot \mathbb{1}(l_3 < \psi_\Delta < u_3)$$

These full conditional distributions do not have a closed form. We use a Metropolis Hastings algorithm to sample these parameters. The proposal densities are

$$q(\phi_U^* \mid \phi_U^{k-1}) \sim N(\phi_U^{k-1}, s_1^2)\mathbb{1}(l_1 < \phi_U^* < u_1)$$
$$q(\psi_U^* \mid \psi_U^{k-1}) \sim N(\psi_U^{k-1}, s_s^2)\mathbb{1}(l_2 < \psi_U^* < u_2)$$
$$q(\psi_\Delta^* \mid \psi_\Delta^{k-1}) \sim N(\psi_\Delta^{k-1}, s_3^2)\mathbb{1}(l_3 < \psi_\Delta^* < u_3)$$

The acceptance ratios are

$$
\begin{aligned}
r_{\phi_U} &= \left(\frac{|\mathbf{R}(\phi_U^*)|}{|\mathbf{R}(\phi_U^{k-1})|} \right)^{-N/2} \exp\left(-\frac{\mathbf{U}^T ((\mathbf{R}(\phi_U^*)^{-1} - \mathbf{R}(\phi_U^{k-1})^{-1}) \otimes \mathbf{R}(\psi_U)^{-1})\mathbf{U}}{2\sigma_U^2} \right) \\
&\quad \cdot \left(\frac{\Phi(\frac{u_1 - \phi_U^{k-1}}{s_1}) - \Phi(\frac{l_1 - \phi_U^{k-1}}{s_1})}{\Phi(\frac{u_1 - \phi_U^*}{s_1}) - \Phi(\frac{l_1 - \phi_U^*}{s_1})} \right) \\
r_{\psi_U} &= \left(\frac{|\mathbf{R}(\psi_U^*)|}{|\mathbf{R}(\psi_U^{k-1})|} \right)^{-M/2} \exp\left(-\frac{\mathbf{U}^T (\mathbf{R}(\phi_U)^{-1} \otimes (\mathbf{R}(\psi_U^*)^{-1} - \mathbf{R}(\psi_U^{k-1})^{-1}))\mathbf{U}}{2\sigma_U^2} \right) \\
&\quad \cdot \left(\frac{\Phi(\frac{u_2 - \psi_U^{k-1}}{s_2}) - \Phi(\frac{l_2 - \psi_U^{k-1}}{s_2})}{\Phi(\frac{u_2 - \psi_U^*}{s_2}) - \Phi(\frac{l_2 - \psi_U^*}{s_2})} \right) \\
r_{\psi_\Delta} &= \left(\frac{|\mathbf{R}(\psi_\Delta^*)|}{|\mathbf{R}(\psi_\Delta^{k-1})|} \right)^{-\frac{1}{2}} \\
&\quad \cdot \exp\left(-\frac{(\log\mathbf{\Delta} - \mathbf{X}\boldsymbol{\beta})^T (\mathbf{R}(\psi_\Delta^*)^{-1} - \mathbf{R}(\psi_\Delta^{k-1})^{-1})(\log\mathbf{\Delta} - \mathbf{X}\boldsymbol{\beta})}{2\sigma_\Delta^2} \right) \\
&\quad \cdot \left(\frac{\Phi(\frac{u_3 - \psi_\Delta^{k-1}}{s_3}) - \Phi(\frac{l_3 - \psi_\Delta^{k-1}}{s_3})}{\Phi(\frac{u_3 - \psi_\Delta^*}{s_3}) - \Phi(\frac{l_3 - \psi_\Delta^*}{s_3})} \right)
\end{aligned}
$$

A.1.1 Adaptive Metropolis Hastings

To sample $\mathbf{\Delta}$, we draw $\log\mathbf{\Delta}$ and take the exponential. The log of the full conditional distribution for $\log\mathbf{\Delta}$ with $\mathbf{U}$ integrated out is

$$
\begin{aligned}
\ell(\log\mathbf{\Delta} \mid \cdot) \propto\ & -\frac{\log\mathbf{\Delta}^T \mathbf{R}(\psi_\Delta)^{-1} \log\mathbf{\Delta} - 2\log\mathbf{\Delta}^T \mathbf{R}(\psi_\Delta)^{-1} \mathbf{X}\boldsymbol{\beta}}{2\sigma_\Delta^2} \\
& -\frac{1}{2}(\mathbf{Z}_\tau\boldsymbol{\alpha} + (\boldsymbol{\epsilon}_\gamma + \boldsymbol{\mu}_R) \circ \mathbf{1}_\tau^+)^T (\sigma_1^2 \mathbf{I}_{MN} + \mathbf{\Sigma}_U)^{-1} (\mathbf{Z}_\tau\boldsymbol{\alpha} + (\boldsymbol{\epsilon}_\gamma + \boldsymbol{\mu}_R) \circ \mathbf{1}_\tau^+).
\end{aligned}
$$

We sample $\mathbf{\Delta} = (\Delta_{s_1}, ..., \Delta_{s_N})^T$ using adaptive component-wise Metropolis Hastings algorithm as follows:

1. Set batch size B. Initialize the log proposal variances ls_i for each spatial components.
2. For $k = 1, ..., K$:
   (a) For $i = 1, ..., N$:
      i. Draw $\log\Delta_{s_i}^*$ from proposal density

$$
q(\log\Delta_{s_i}^* \mid \log\Delta_{s_i}^{k-1}) \sim N(\log\Delta_{s_i}^{k-1}, \exp(ls_i)).
$$

      ii. Calculate acceptance ratio

$$
\begin{aligned}
r = \exp(& -(\log\mathbf{\Delta}^* - \log\mathbf{\Delta}^{k-1})^T \mathbf{R}(\psi_\Delta)^{-1} (\log\mathbf{\Delta}^* + \log\mathbf{\Delta}^{k-1} - \mathbf{X}\boldsymbol{\beta})/2\sigma_\Delta^2 + \\
& (\boldsymbol{\mu}_\tau^* + \boldsymbol{\mu}_\tau^{k-1} + \boldsymbol{\epsilon}_\gamma \circ (\mathbf{1}_\tau^{+*} + \mathbf{1}_\tau^{+k-1}) - 2(\mathbf{Y} - \mathbf{U}))^T \\
& (\boldsymbol{\mu}_\tau^* - \boldsymbol{\mu}_\tau^{k-1} + \boldsymbol{\epsilon}_\gamma \circ (\mathbf{1}_\tau^{+*} - \mathbf{1}_\tau^{+k-1})/2\sigma_1^2)),
\end{aligned}
$$

where

$$
\mathbf{\Delta}^* = (\Delta_{s_1}^k, ..., \Delta_{s_{i-1}}^k, \Delta_{s_i}^*, \Delta_{s_{i+1}}^{k-1}, ..., \Delta_{s_N}^{k-1})^T,
$$

and

$$
\mu_\tau^*(\mathbf{s}, t) = \alpha_0 + [\gamma_0(\mathbf{s}) + \gamma_1(\mathbf{s}) \cdot (t - \tau_0 - \Delta^*(\mathbf{s}))] \cdot \mathbb{1}(t > \tau_0 + \Delta^*(\mathbf{s})).
$$

iii. Sample $u \sim Unif(0,1)$. Set $\Delta^k = \begin{cases} \Delta^* & \text{if } r > u \\ \Delta^{k-1} & o.w. \end{cases}$. Set $a^k = \begin{cases} 1 & \text{if } r > u \\ 0 & o.w. \end{cases}$.

(b) If $k = jB$ for integer $j \geq 1$:

    i. Calculate the average acceptance rate for the jth batch as $a_j = \sum_{l=k-B+1}^{k} a^l / B$.

    ii. Update $ls_i = \begin{cases} ls_i + \Delta(j), & a_j > 0.44 \\ ls_i - \Delta(j), & a_j \leq 0.44, \end{cases}$
        where $\Delta(j) = \min(0.1, 1/\sqrt{j})$.

The full conditional for $\boldsymbol{\gamma_{0R}}$ is

$$\mathbf{1}_M \otimes \boldsymbol{\gamma_{0R}} \sim N(\widetilde{\boldsymbol{\mu}}_{\boldsymbol{\gamma_0}}, \widetilde{\boldsymbol{\Sigma}}_{\boldsymbol{\gamma_0}}),$$

where

$$\widetilde{\boldsymbol{\Sigma}}_{\boldsymbol{\gamma_0}} = \frac{diag(\mathbf{1}_\tau^+)}{\sigma_1^2} + \mathbf{I}_N \otimes \boldsymbol{\Sigma}_{\boldsymbol{\gamma_0}},$$

$$\widetilde{\boldsymbol{\mu}}_{\boldsymbol{\gamma_0}} = \widetilde{\boldsymbol{\Sigma}}_{\boldsymbol{\gamma_0}}^{-1} \left(\frac{diag(\mathbf{1}_\tau^+)(\mathbf{Y} - \boldsymbol{\mu}_\tau - \boldsymbol{\epsilon}_\gamma)}{\sigma_1^2} \right).$$

Since $diag(\mathbf{1}_\tau^+)$ is not separable, there is no easy way to sample from this distribution directly. Thus, we use the adaptive component-wise Metropolis Hastings to update $\boldsymbol{\gamma_{0R}}$ instead of using a Gibbs Sampler. The steps for updating $\boldsymbol{\gamma_{0R}}$ and $\boldsymbol{\gamma_{1R}}$ are same as Δ, where the acceptance ratio for $\boldsymbol{\gamma_{0R}}$ is given by

$$r = \exp\left(- (\boldsymbol{\gamma_{0R}}^* + \boldsymbol{\gamma_{0R}}^{k-1})^T \boldsymbol{\Sigma}_{\boldsymbol{\gamma_0}}^{-1} (\boldsymbol{\gamma_{0R}}^* - \boldsymbol{\gamma_{0R}}^{k-1})/2 + \right.$$
$$\left. ((\mathbf{1}_M \otimes (\boldsymbol{\gamma_{0R}}^* + \boldsymbol{\gamma_{0R}}^{k-1})) \circ \mathbf{1}_\tau^+ - 2\mathbf{A})^T ((\mathbf{1}_M \otimes (\boldsymbol{\gamma_{0R}}^* - \boldsymbol{\gamma_{0R}}^{k-1})) \circ \mathbf{1}_\tau^+)/2\sigma_1^2 \right),$$

where

$$\mathbf{A} = \mathbf{Y} - \mathbf{U} - \boldsymbol{\mu}_F - \boldsymbol{\gamma_{1R}} \circ (\mathbf{t} \otimes \mathbf{1_N} - \mathbf{1_M} \otimes \boldsymbol{\tau}),$$

and the acceptance ratio for $\boldsymbol{\gamma_{1R}}$ is given by

$$r = . \exp(-(\boldsymbol{\gamma_{1R}}^* + \boldsymbol{\gamma_{1R}}^{k-1})^T \boldsymbol{\Sigma}_{\boldsymbol{\gamma_1}}^{-1} (\boldsymbol{\gamma_{1R}}^* - \boldsymbol{\gamma_{1R}}^{k-1})/2 +$$
$$((\mathbf{1}_M \otimes (\boldsymbol{\gamma_{1R}}^* + \boldsymbol{\gamma_{1R}}^{k-1})) \circ (\mathbf{t} \otimes \mathbf{1_N} - \mathbf{1_M} \otimes \boldsymbol{\tau}) \circ \mathbf{1}_\tau^+ - 2\mathbf{A})^T$$
$$((\mathbf{1}_M \otimes (\boldsymbol{\gamma_{1R}}^* - \boldsymbol{\gamma_{1R}}^{k-1})) \circ (\mathbf{t} \otimes \mathbf{1_N} - \mathbf{1_M} \otimes \boldsymbol{\tau}) \circ \mathbf{1}_\tau^+)/2\sigma_1^2),$$

where

$$\mathbf{A} = \mathbf{Y} - \mathbf{U} - \boldsymbol{\mu}_F - \boldsymbol{\gamma_{0R}}.$$
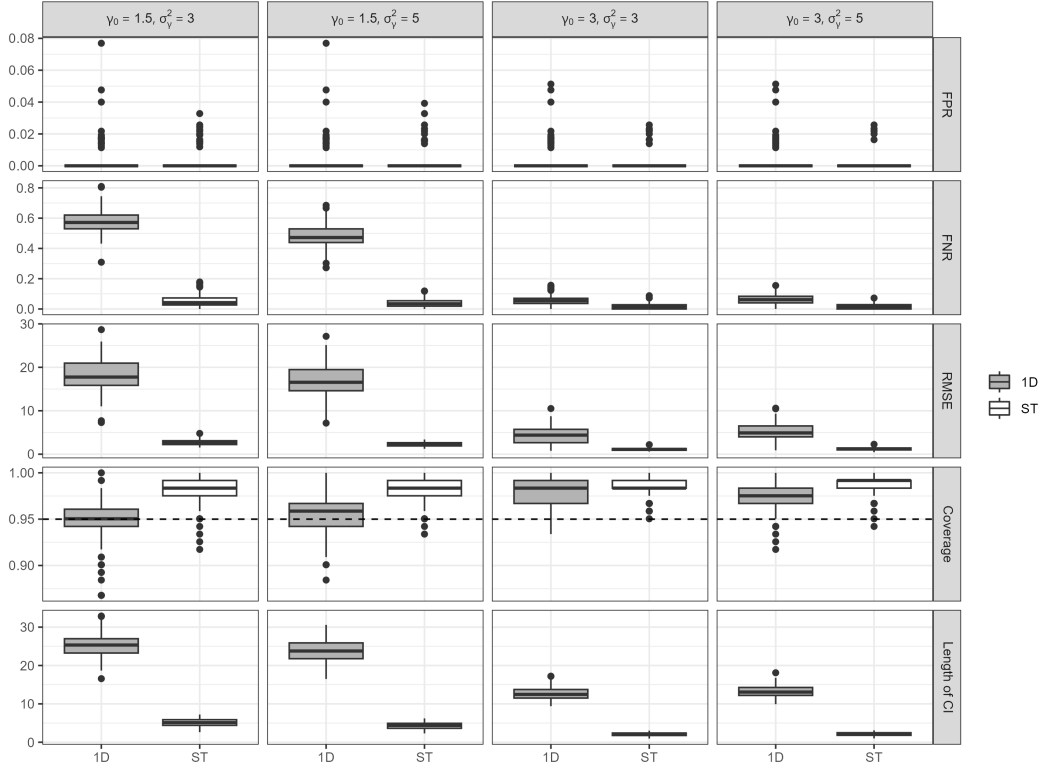
B   Tables and Figures

Fig. 10: Boxplots of RMSE, FPR, FNR, the empirical coverage probability and the length of 95% credible intervals under $\gamma_0 \in \{1.5, 3\}$ and $\sigma_\gamma^2 \in \{3, 5\}$. "ST" is our spatio-temporal model and "1D" is the univariate method.
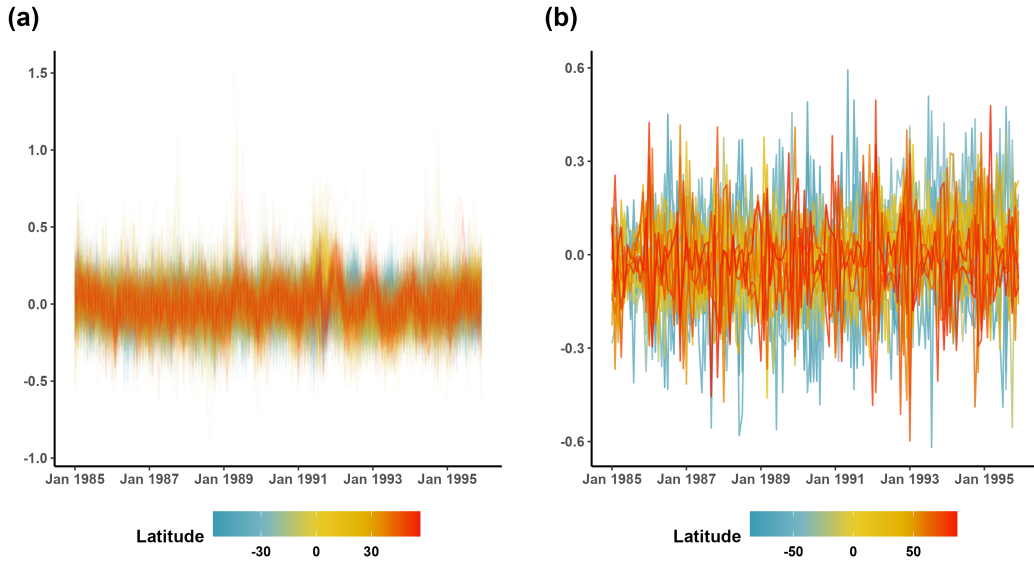

Fig. 11: Residual plot of (a) stratospheric AOD and (b) surface temperature under $\sigma_1^2 = \sigma_2^2$

Latitude	Posterior Mode	$\mathbb{P}$(no changepoint)	95% CI
86.0°S	Dec 1995 (No CP)	0.9905	(Dec 1995, Dec 1995)
78.5°S	Dec 1995 (No CP)	0.9888	(Dec 1995, Dec 1995)
71.0°S	Dec 1995 (No CP)	0.9762	(Dec 1995, Dec 1995)
63.5°S	Dec 1995 (No CP)	0.7955	(Apr 1992, Dec 1995)
56.0°S	Mar 1992	0.0037	(Jul 1991, Jul 1994)
48.5°S	Oct 1991	0	(Jul 1991, Feb 1992)
41.0°S	Sep 1991	0	(Jul 1991, May 1992)
33.5°S	Sep 1991	0.0001	(Jul 1991, Jan 1992)
26.0°S	Oct 1991	0.0112	(Jun 1991, Nov 1992)
18.5°S	Dec 1995 (No CP)	0.8470	(Apr 1995, Dec 1995)
11.0°S	Sep 1991	0	(Aug 1991, Aug 1992)
3.5°S	Apr 1992	0	(Aug 1991, Sep 1991)
4.0°N	May 1992	0	(Oct 1991, Aug 1992)
11.5°N	Sep 1991	0	(Jul 1991, Dec 1991)
19.0°N	Sep 1991	0	(Jun 1991, Nov 1991)
26.5°N	Dec 1995 (No CP)	0.9878	(Dec 1995, Dec 1995)
34.0°N	Dec 1995 (No CP)	0.9763	(Dec 1995, Dec 1995)
41.5°N	Sep 1991	0	(Jul 1991, Jun 1992)
49.0°N	Sep 1991	0	(Jul 1991, Mar 1992)
56.5°N	Dec 1995 (No CP)	0.9788	(Dec 1995, Dec 1995)
64.0°N	Dec 1995 (No CP)	0.9986	(Dec 1995, Dec 1995)
71.5°N	Dec 1995 (No CP)	0.9984	(Dec 1995, Dec 1995)
79.0°N	Dec 1995 (No CP)	0.9943	(Dec 1995, Dec 1995)
86.5°N	Dec 1995 (No CP)	0.9984	(Dec 1995, Dec 1995)

Table 4: Summary of detected changepoints for surface temperature